Nonlinear Dyn (2025) 113:24077–24100
https://doi.org/10.1007/s11071-025-11104-4

RESEARCH

# A new strategy for vibration suppression in locally resonant metamaterials based on autoparametric resonance

**Xiao Wang · Jianlei Zhao · Ivana Kovacic · Honggang Li · Runan Hua · Rui Zhu**

Received: 30 September 2024 / Accepted: 8 March 2025 / Published online: 27 March 2025


**Abstract** Locally resonant metamaterials can achieve vibration suppression within a certain bandgap range. However, even a slight deviation between the excitation frequency and the bandgap range can cause large amplitude response due to the resonant peaks near the linear bandgap region. To overcome this issue, nonlinear locally resonant metamaterials shift the resonance peaks through hardening or softening stiffness, effectively weakening the intensity of the resonance and broadening the vibration attenuation range. Different from such conventional nonlinear locally resonant metamaterials, this paper integrates the concepts of dynamic vibration absorbers and autoparametric vibration absorbers, proposing a novel nonlinear locally resonant metamaterial based on autoparametric resonance. This paper begins by deriving the system's governing equations through the extended Hamilton's principle while considering the effects of geometric nonlinearity. Then, the nonlinear vibration suppression characteristics of the unit cell and metamaterial are investigated. It is found that the autoparametric resonance-based metamaterial not only preserves the original linear bandgap but also suppresses the resonant peaks near the bandgap, generating a new adjustable nonlinear vibration attenuation region at the lower frequency. Besides, the effect of damping is also examined, demonstrating that reducing damping can further enhance the vibration suppression within the nonlinear range. Finally, by employing the gradient design of the absorbers' natural frequency, the nonlinear attenuation regions and linear bandgap are merged, effectively broadening the range of vibration suppression. The study shows that metamaterials based on the autoparametric resonance mechanism can overcome the limitations of the existing locally resonant metamaterials, providing a new strategy and insights for resonance suppression in periodic structures.

**Keywords** Nonlinear metamaterials · Vibration attenuation · Resonance peak suppression · Autoparametric resonance

X. Wang · J. Zhao · R. Zhu (✉)
School of Aerospace Engineering, Beijing Institute of Technology, Beijing 100081, China
e-mail: ruizhu@bit.edu.cn

I. Kovacic (✉)
Faculty of Technical Sciences, Centre of Excellence for Vibro-Acoustic Systems and Signal Processing CEVAS, University of Novi Sad, Novi Sad, Serbia
e-mail: ivanakov@uns.ac.rs

H. Li · R. Hua
Wuhan Second Ship Design and Research Institute, Wuhan 430064, China

## 1 Introduction

Metamaterials are artificially synthesized materials that, through the design of periodic microstructure,

break the mechanical performance limitations of materials, exhibiting properties beyond those of natural materials [1]. The unit design of metamaterial is highly flexible, allowing them to be either discrete mechanisms or continuous structures, tailored to address various practical problems and achieve different functions [2]. So far, metamaterials have been applied in many fields, including waveguides [3, 4], cloaking [5, 6], nondestructive testing [7, 8], energy absorption and harvesting [9–11]. One of the important applications of metamaterials is to achieve broad low-frequency vibration attenuation. Locally resonant metamaterials (LRMs) form bandgaps near the resonators' natural frequencies [12]. Within the bandgap, energy is blocked by out-of-phase resonant motions of the periodically arranged resonators, thereby effectively suppressing the global propagation of vibrations [13]. Different from the Bragg scattering mechanism in phononic crystals, customable bandgap can be generated solely determined by the local resonators, which provides an advantage of achieving low-frequency vibration attenuation on a small-scale metastructure [14]. To further explain the formation mechanism of the locally resonant bandgap, Huang et al. [15] constructed one-dimensional mass-in-mass lattices and discovered that the negative effective mass results in the attenuation of wave amplitude along the metamaterial. For a unit cell of LRM, the concept of negative effective mass can be understood through the perspective of a dynamic vibration absorber (DVA) [16]. When the excitation frequency is greater than or equal to the resonant frequency, the effective mass is negative within a certain range. The negative effective mass corresponds to the system's optical mode, where the resonator vibrates out of phase with the primary mass, and the counteracting force of the resonator reduces the amplitude of the primary mass [17]. However, both LRM and DVA indicate that the bandgap of LRMs is very narrow and more resonance peaks are also generated near the bandgap region due to the modal vibrations of the resonators, making it impossible to achieve vibration attenuation over a broadband range. In order to broaden the attenuation range, unit cells with varying resonator designs need to be added. Pai et al. [18, 19] designed metamaterial beams with gradiently changing local resonators. Zhu et al. [20] designed a chiral elastic metamaterial beam with section-arranged different resonators, which effectively attenuates vibrations over a wide frequency range by eliminating dynamic interactions between the resonators. However, due to structural size limitations, the overall mass of the resonators has to be increased. Rui et al. [21] proposed an vibration-absorbing metamaterial with a two-degree-of-freedom unit that achieves multi-band and multi-mode vibration suppression. Owing to the drawbacks of the vibration absorption mechanism, new resonance peaks still appear on both sides of the absorption frequencies. In addition, the use of various locally resonant attenuation bands can also achieve wideband vibration control. Dwivedi et al. [22] proposed a double-negative metabeam by combining the negative stiffness and mass, which significantly broadens the vibration suppression range by merging bandgaps at different frequencies. For the traditional LRMs, broadening the suppression range often requires increasing the resonator mass or damping, which is detrimental to the lightweight design and the damping effect is poor for low frequency vibration. Additionally, excessive damping can diminish the suppression effect within the bandgap and may even cause the bandgap to close [23].

To overcome the limitations of linear systems, nonlinear springs with softening or hardening stiffness are incorporated into the linear system [24]. For nonlinear dynamic vibration absorbers (NDVAs), incorporating nonlinearity causes the resonance peak to bend, thereby reducing its amplitude and widening the vibration suppression range [25, 26]. Nonlinear locally resonant metamaterials (NLRMs) constructed with NDVAs as unit cells exhibit various interesting wave propagation phenomena, offering potential for broadening the linear bandgap [27, 28]. Fang et al. [29, 30] introduced a local bifurcation mechanism to eliminate multimodal resonances in the original passband, generating new chaotic bands that achieve broadband vibration suppression. Compared to linear systems, nonlinearity can significantly enhance the influence of the mass ratio on the bandgap, necessitating less additional mass to achieve a broader nonlinear suppression range [31]. Meanwhile, NLRMs demonstrate strong amplitude dependence, such that increasing the excitation amplitude can significantly enhance the system's nonlinearity. At different levels of nonlinearity, NLRMs can exhibit both linear and nonlinear vibration attenuation mechanisms [32]. Xiao et al. [33] increased the excitation amplitude to enhance the strength of nonlinearity,

achieving a wider range of vibration attenuation through the bistable mechanism. Furthermore, nonlinear designs are more flexible and adaptable. Zhao et al. [34] used triplets of resonators and broadened the linear bandgap through a combination of hardening-plus-softening nonlinearity. Yu et al. [35] designed a combination of linear and nonlinear metamaterials, greatly improving the bandwidth and robustness of vibration suppression. Chen et al. [36] incorporated fractional and cubic nonlinearities through circuit design, achieving wideband suppression at a lower excitation amplitude threshold. Zhao et al. [37] proposed bi-linear oscillators based on non-smooth nonlinearity, which suppress the amplitude of resonance peaks on both sides of the bandgap through chaotic effects. For most NLRMs, although the amplitude of the resonance peaks is attenuated, the resonator's single vibration mode is insufficient to completely eliminate the resonance peaks. Furthermore, the nonlinear and linear systems affect each other and cannot be adjusted independently.

Unlike the aforementioned nonlinear mechanisms, autoparametric resonance is a completely different nonlinear vibration phenomenon, not caused by external excitation, but by time-varying changes in system's parameters [38, 39]. A key characteristic of an autoparametric vibration system is nonlinear internal coupling, which involves at least two modes. When the natural frequencies of the two modes are in a two-to-one ratio, energy is transferred from one mode to another one [40, 41]. Therefore, autoparametric resonance is often used to suppress vibrations induced by resonant or near-resonant excitations. Haxton et al. [42] attached cantilever beams with tip masses to the base structure, proposing an autoparametric vibration absorber (AVA). Experimental results demonstrate that this absorber is highly effective in suppressing the resonant response. Subsequently, Yan et al. [43] expanded on this by employing the method of multiple scales (MMS) to analyze the stability and bifurcation of the system, discovering various nonlinear phenomena, such as saturation, jumps, hysteresis, and chaos. Compared to DVA, the AVA's vibration direction is perpendicular to that of the primary system, and when it is not close to the main system's resonant frequency, the AVA does not cause undesirable resonance. However, the vibration absorption frequency range of a single AVA remains narrow. Vyas et al. [44] extended the suppression range of the resonant response by attaching multiple pendulums with varying natural frequencies to a single-degree-of-freedom system. Although the advantage of inducing autoparametric resonance is obvious, particularly for suppressing the resonance peaks of the global structures, the research on autoparametric resonance in the field of metamaterials is limited. Yu et al.[45] and Zhou et al. [46] integrated autoparametric resonance with nonlinear chirality and nonlinear inertia respectively, to achieve non-reciprocal wave propagation within periodic structures. Silva et al. [47] produced internal resonance via nonlinear wave interactions, resulting in a subharmonic attenuation zone. However, due to the limitations of quadratic nonlinearity, this new nonlinear attenuation zone can only manifest at twice the locally resonant frequency.

In order to effectively suppress the resonance peaks near the linear bandgap region and further enhance the vibration suppression capability of LRMs, we propose a novel NLRM that leverages the vibration absorption mechanisms of both DVA and AVA. It not only preserves the original band gap but also effectively weakens the resonant peaks near the bandgap, generating a new nonlinear attenuation region at low frequencies. Furthermore, through parameter design, the linear and nonlinear bandgaps have been successfully merged, significantly broadening the suppression range. The paper is organized as follows. Section 2 presents the mechanical and mathematical models of the nonlinear unit cell, as well as the corresponding governing equations through the extended Hamilton's principle. Section 3 explores the impact of autoparametric resonance on vibration suppression in both the unit cell and the metamaterial as a whole, elucidating the suppression mechanism by parameter analyses, while verifying them through finite element simulations. Additionally, the parameter design for metamaterials to achieve improved suppression performances are presented in Sect. 4. Finally, the conclusions are summarized in Sect. 5.

## 2 Mechanical and mathematical models

First, the proposed autoparametric resonance-based metamaterials (ARMs) are shown in Fig. 1a. Compared with traditional linear LRMs, the unit cell of the ARMs considered herein consists of three parts: a bottom block $M_1$, a cantilever beam and a tip block

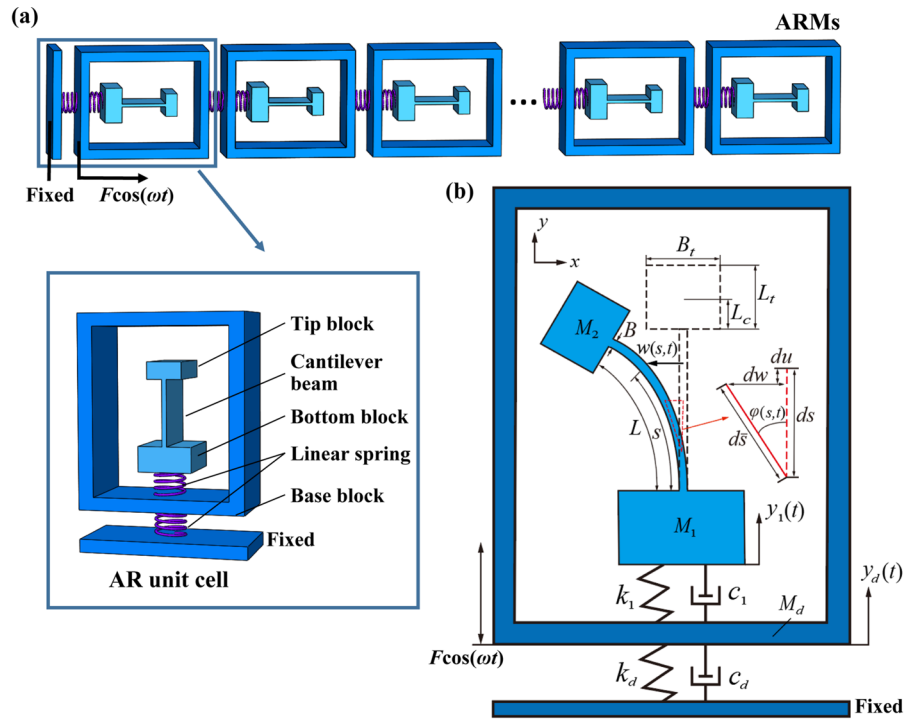


**Fig. 1** **a** The conceptual design of the proposed autoparametric resonance-based metamaterials (ARMs). The unit cells are connected by linear springs. The enlarged view shows the components of the unit cell; **b** Mechanical model of the three-degree-of-freedom AR unit cell. The dashed line represents the undeformed state, while the solid line represents the deformed state. The schematic on the right-hand side is used to define the geometry and illustrate the in-extensibility condition

$M_2$. The tip block and the bottom block are connected by a cantilever beam capable of undergoing bending deformation. As shown in Fig. 1b, the stiffness and damping of the linear springs connecting the bottom block to the movable base (frame) of block $M_d$ and the movable base to the fix one are $k_1$, $c_1$ and $k_d$, $c_d$, respectively. The length, width and moment of inertia of the tip block are $L_t$,$B_t$ and $J_t$, respectively. The length and width of the cantilever beam are $L$ and $B$. The distance from the centre of tip block to the cantilever beam's free end is denoted by $L_c$. The bottom of the unit cell is fixed, and a harmonic force excitation is applied to the base block in the $y$ direction. The position of the tip block and bottom block are respectively defined by the generalized coordinates $y_d$ and $y_1$. The displacement and rotation angle of the cantilever beam in the deflection direction are $w(s,t)$ and $\varphi(s,t)$, respectively, where $s$ is the local coordinate along the neutral axis of the cantilever beam and $t$ is the time. It is assumed that the cantilever beam is an Euler–Bernoulli beam, and there is no axial deformation after large deformation, i.e., the beam is inextensible [48].

Figure 1b illustrates the geometric relationship of cantilever beam deformation. The red dashed line represents the initial undeformed state (length d$s$), and the red solid line represents the deformed state (length d$\bar{s}$). Considering the in-extensibility condition, the infinitesimal length d$s$ remains unchanged before and after beam bending. Furthermore, we assume that d$s$ = d$\bar{s}$[49], and the geometric relationship is as follows:

$$\sin\varphi = \frac{\mathrm{d}w}{\mathrm{d}\bar{s}} = \frac{\mathrm{d}w}{\mathrm{d}s} = w' \tag{1}$$

$$(\mathrm{d}s - \mathrm{d}u)^2 + \mathrm{d}w^2 = \mathrm{d}\bar{s}^2 = \mathrm{d}s^2 \tag{2}$$

where d$u$ and d$w$ represent the infinitesimally small displacement in the $y$ and $x$ direction, respectively. Considering the geometric relationship of the beam, the components of $\varphi\prime(s,t)$ and $u\prime(s,t)$ are expressed as follows:

$$\begin{aligned}\frac{\mathrm{d}\varphi(s,t)}{\mathrm{d}s} &= \left(\sin^{-1}(w'(s,t))\right)' \\ &\approx w''(s,t)\left(1+\frac{1}{2}w'(s,t)^2\right)\end{aligned} \tag{3}$$

$$\frac{\mathrm{d}u(s,t)}{\mathrm{d}s} = 1 - \cos\varphi(s,t) \approx \frac{w'(s,t)^2}{2} \tag{4}$$

In Eq. (3) and (4), the simplification is performed using the Taylor expansion. Terms of the third and

higher orders are neglected due to their negligible impact on the results. To further obtain the governing equation of the proposed system, we choose the extended Hamilton's principle [50]:

$$\int_{t_1}^{t_2} (\delta T - \delta \Pi + \delta W_{nc}) \mathrm{d}t = 0 \tag{5}$$

where $(t_1, t_2)$ is arbitrary time span. $T$, $\Pi$ and $W_{nc}$ are respectively the kinetic energy, potential energy and virtual work due to non-conservative forces.

Then, by substituting the geometric relationships Eq. (3) and (4), the potential energy $\Pi$ and kinetic energy $T$ are expressed as

$$\begin{aligned} \mathit{II} = & \frac{1}{2} k_d y_d^2 \\ & + \frac{1}{2} k_1 (y_1 - y_d)^2 + \int_0^L \frac{1}{2} EI \left[ w''^2 + w''^2 w'^2 \right] ds \end{aligned} \tag{6a}$$

$$\begin{aligned} T = & \frac{1}{2} M_d \dot{y}_d(t)^2 + \frac{1}{2} M_1 \dot{y}_1(t)^2 + \frac{1}{2} J_t \int_0^L \left( \frac{\partial}{\partial t} \left( w' + \frac{w'^3}{6} \right) \right)^2 \delta(s - L) ds \\ & + \frac{1}{2} \int_0^L \rho \left[ \dot{y}_1(t) - \frac{d}{dt} \left( \int_0^s \frac{1}{2} \left( \frac{\partial w(\eta, t)}{\partial \eta} \right)^2 d\eta \right) \right]^2 ds + \frac{1}{2} \int_0^L \rho \dot{w}^2 ds \\ & + \frac{1}{2} M_2 \left( \dot{w}(L, t) + \int_0^L L_c \dot{w}' \left( 1 + \frac{1}{2} w'^2 \right) \left( 1 - \frac{1}{2} w'^2 \right) \delta(s - L) ds \right)^2 \cdot \\ & + \frac{1}{2} M_2 \left[ \dot{y}_1(t) - \frac{d}{dt} \left( \int_0^L \frac{1}{2} \left( \frac{\partial w(\eta, t)}{\partial \eta} \right)^2 d\eta \right) \right. \\ & \left. + \int_0^L L_c w' \dot{w}' \left( 1 + \frac{1}{2} w'^2 \right) \delta(s - L) ds \right]^2 \end{aligned} \tag{6b}$$

where the dot $(\cdot)$ represents the derivative with respect to $t$, while $\rho$ and $EI$ are the mass per unit length and the bending stiffness of the beam, respectively. For Eq. 6a, the first and second terms on the right-hand side represent the potential energy of two linear springs, while the third term corresponds to the bending strain energy of the cantilever beam. For Eq. 6b, the first and second terms on the right-hand side represent the kinetic energy of the base block and bottom block, respectively. The third term corresponds to the rotational kinetic energy of the tip block. The fourth and fifth terms represent the kinetic energy of the cantilever beam in the $y$ and $x$ directions, respectively. The sixth and seventh terms correspond to the kinetic energy of the tip block in the $x$ and $y$ directions, respectively. Here, we ignore the effect of gravity on potential energy and the effect of beam mass on kinetic energy.

In the kinetic energy term, the motions defined by the generalized coordinates $y_1(t)$ and $w(s, t)$ are coupled to each other in the $y$ direction, resulting in a nonlinear effect on $M_1$. In the expression, the geometric nonlinearity of the beam deformation and the influence of the structural dimensions of tip block are considered. The terms containing $L_c$ and $J_t$ represent the effects of the position of the center and the rotation of the tip block on the system's kinetic energy, respectively. When the deformation of the beam is significant, the influence of the rotation angle $\varphi(s, t)$ increases. Therefore, we retain terms up to the third order $w\prime(s, t)^3$ and below in the expansion.

Further, the work stemming from non-conservative terms includes damping forces of the spring and cantilever beam, as well as external excitation, and is expressed as

$$\begin{aligned} W_{nc} = & \oint F_d(t) \mathrm{d}y_d + \oint F_1(t) \mathrm{d}y_1 \\ & + \int_0^L \oint F_2(s, t) \mathrm{d}w \mathrm{d}s + F(t) y_d(t) \end{aligned} \tag{7}$$

where $F_d(t)$ and $F_1(t)$ are the damping forces generated by the linear viscous dampers, acting on base block and bottom block respectively, the expressions for which are $F_d = -c_d \frac{\partial y_d(t)}{\partial t}$ and $F_1 = -c_1 \frac{\partial y_1(t)}{\partial t}$. $F_2$ is the structural damping force generated by the cantilever beam, which is assumed to be linear as well, and its expression can be written as [51] $F_2 = c \frac{\partial w(s,t)}{\partial t}$, where $c$ represents the viscous damping coefficient. The last term in Eq. (7) $F(t)$ is the harmonic force applied to the base block and it is assumed to be of the form $F(t) = F\cos(\omega t)$, where $F$ is the excitation amplitude and $\omega$ is the excitation angular frequency.

Substituting the expressions for the kinetic energy $T$, potential energy $\Pi$ and virtual work $W_{nc}$ into Eq. (5), and performing some simplification, the governing equations of the three-degree-of-freedom AR unit cell can be expressed as follows

$$M_d\ddot{y}_d + c_d\dot{y}_d + c_1(\dot{y}_d - \dot{y}_1) + k_d y_d + k_1(y_d - y_1) = F\cos(\omega.t) \tag{8a}$$

$$(M_1 + M_2 + M_c)\ddot{y}_1 + c_1(\dot{y}_1 - \dot{y}_d) + k_1(y_1 - y_d) - \int_0^L M_2\left(\frac{1}{2}\frac{d^2}{dt^2}(w)'^2 + \frac{L_c}{2}\frac{d^2}{dt^2}(w)'^2\delta(s-L)\right)ds - \int_0^L \rho\int_0^s \frac{d^2}{dt^2}\left[\frac{1}{2}\left(\frac{dw(\eta,t)}{d\eta}\right)^2\right]d\eta ds = 0 \tag{8b}$$

$$\begin{aligned}&\rho\ddot{w} + EI[w'''' + w'^2w'''' + w''^3 + 4w'w''w'''] + c\dot{w}\\ &+\left\{\begin{array}{l} M_2\left(\int_0^s \frac{d^2}{dt^2}\left[\frac{1}{2}\left(\frac{dw(\eta,t)}{d\eta}\right)^2\right]d\eta - L_c\frac{d^2}{dt^2}(w')^2\right)\delta(s-L) + \rho\int_0^s \frac{d^2}{dt^2}\left[\frac{1}{2}\left(\frac{dw(\eta,t)}{d\eta}\right)^2\right]d\eta \\ -\rho\ddot{y}_1 - M_2\ddot{y}_1\left(\delta(s-L) + L_c\frac{d\delta(s-L)}{ds}\right) + J_t\left(\frac{1}{2}\frac{d^2}{dt^2}(w')^2\frac{d\delta(s-L)}{ds} - \alpha\delta(s-L)\right)\end{array}\right\}w'\\ &+\left\{\begin{array}{l}[M_2(1 + L_c\delta(s-L)) + \rho(L-s)]\ddot{y}_1 - \int_s^L \rho\int_0^\xi \frac{d^2}{dt^2}\left(\frac{dw(\eta,t)}{d\eta}\right)^2 d\eta d\xi \\ -M_2\left(\int_0^L\left(\frac{d^2}{dt^2}\frac{1}{2}(w')^2 - L_c\frac{d^2}{dt^2}(w')^2\delta(s-L)\right)ds\right) - \frac{J_t}{2}\frac{d^2}{dt^2}(w')^2\delta(s-L)\end{array}\right\}w'' = 0\end{aligned} \tag{8c}$$

In Eq. (8b), $M_c$ is the total mass of the cantilever beam given by $M_c = \int_0^L \rho ds$, and $\delta(s-L)$ is the Dirac delta function. In Eq. (8c), one has $\alpha = \ddot{w}'w'' + 2\dot{w}'\dot{w}'' + w'\ddot{w}''$, and the coefficient before the $w''$ term is expressed as the axial force applied at different positions on the beam. Moreover, when the mass of the tip block increases, the influence of its centre offset distance $L_c$ and moment of inertia $J_t$ also increases. Therefore, we consider their impact on the structural nonlinearity, resulting in a more accurate vibration response.

As the excitation on the base block is harmonic, in order to further characterize the nonlinear response of the AR unit cell, we use the Galerkin approach to discretize the motion of the cantilever beam, so as to calculate the natural frequencies and modes of different orders. Based on the modal superposition method [52], it is assumed that the deflection $w(s,t)$ is a uniformly convergent series:

$$w(s,t) = \sum_{i=1}^{\infty}\phi_i(s).q_i(t) \tag{9}$$

where $q_i(t)$ and $\phi_i(s)$ are time and spatial variables, representing the i-th modal coordinates and modal shapes of the cantilever beam with tip block. Then the modal shape $\phi_i(s)$ of beam can be expressed as

$$\phi_i(s) = A_i\sin\beta_i s + B_i\cos\beta_i s + C_i\sinh\beta_i s + D_i\cosh\beta_i s \tag{10}$$

where $A_i$, $B_i$, $C_i$ and $D_i$ are the coefficients that can be calculated from the boundary, equation, while $\beta_i$ are unknown eigenvalues.

For the cantilever beam with the tip block, the simplified boundary conditions are taken as follows [53]:

$$\begin{cases}\phi(0) = 0\\ \phi'(0) = 0\\ EI\phi''(L) - \omega^2M_2L_c\phi(L) - \omega^2J_t\phi'(L) = 0\\ EI\phi'''(L) + \omega^2M_2L_c\phi'(L) + \omega^2M_2\phi(L) = 0\end{cases} \tag{11}$$

Substituting Eq. (10) into Eq. (11), we can further obtain $\beta_i$ by solving the following eigenvalue equation:

$$
\begin{aligned}
&J_t M_2 \frac{\beta_i^4}{\rho} + \rho - M_2^2 \frac{\beta_i^4}{\rho} L_c^2 - \beta_i \sin(L\beta_i) \\
&\left(\left(M_2 + J_t\beta_i^2\right)\cosh(L\beta_i) + 2\beta M_2 \sinh(L\beta_i)L_c\right) \\
&+ \cos(L\beta_i)\left(\beta_i\left(M_2 - J_t\beta_i^2\right)\sinh(L\beta_i) + \cosh(L\beta_i)\right. \\
&\left.\left(-J_t M_2 \frac{\beta_i^4}{\rho} + M_2^2 \frac{\beta_i^4}{\rho} L_c^2 + \rho\right)\right) = 0
\end{aligned} \tag{12}
$$

Furthermore, based on the orthogonality conditions, the eigenvectors are normalized by the following expression [54]

$$
\begin{cases}
\int_0^l \rho\phi_i(s)\phi_j(s)ds + M_2\phi_i(L)\phi_j(L) + J_t\phi_i'(L)\phi_j'(L) + M_2L_c\phi_i(L)\phi_j'(L) + M_2L_c\phi_i'(L)\phi_j(L) = \delta_{ij} \\
\int_0^l EI\phi_i''(s)\phi_j''(s)ds = \delta_{ij}\omega_i^2
\end{cases} \tag{13}
$$

where $i$ and $j$ represent the vibration modes of different orders;$\delta_{ij}$ is the Kronecker delta, defined as unity when $i$ is equal to $j$ and zero otherwise. Moreover,$\omega_i$ is the i-th undamped natural angular frequency, as given by

$$
\omega_i = \beta_i^2\sqrt{EI/\rho} \tag{14}
$$

Since the second and third order natural frequencies are much larger than the first order natural frequency, only the first-order modes of the beam system are used herein to calculate the corresponding response. The coefficients $A_i$, $B_i$, $C_i$ and $D_i$ in Eq. (10) are obtained by considering Eq. (11–13). Subsequently, Eq. (9) is substituted into Eq. (8). Then, Eq. (8c) is multiplied by the first-order mode shape $\phi_1(s)$, and integrated along the length of the beam. Finally, the dimensionless governing equations of the AR unit cell is obtained in the form:

$$
\begin{aligned}
&\ddot{y}_d + 2\xi_d\omega_d\dot{y}_d + 2\xi_1\gamma_1\mu(\dot{y}_d - \dot{y}_1) + \omega_d^2 y_d + \gamma_1^2(y_d - y_1) = A\cos(\omega t) \\
&\ddot{y}_1 + 2\xi_1\omega_1(\dot{y}_1 - \dot{y}_d) + \omega_1^2(y_1 - y_d) - \frac{n_3}{M_1 + M_2 + M_c}\left(q\ddot{q} + \dot{q}^2\right) = 0 \\
&\ddot{q} + 2\xi_2\omega_2\dot{q} + \omega_2^2 q + n_1q^3 + n_2q(q\ddot{q} + \dot{q}^2) - n_3q\ddot{y}_1 = 0
\end{aligned} \tag{15}
$$

where

$$
\begin{aligned}
&\omega_d = \sqrt{\frac{k_d}{M_d}};\ \omega_1 = \sqrt{\frac{k_1}{M_1 + M_2 + M_c}}; \\
&\gamma_1 = \sqrt{\frac{k_1}{M_d}};\ A = \frac{F}{M_d};\ \mu = \sqrt{\frac{M_1 + M_2 + M_c}{M_d}} \\
&\xi_d = \frac{c_d}{2M_d\omega_d};\ \xi_1 = \frac{c_1}{2(M_1 + M_2 + M_c)\omega_1};\ \xi_2 = \frac{c\int_0^L \phi_1^2(s)ds}{2\omega_2}
\end{aligned} \tag{16}
$$

In Eq. (15), $\omega_1$ and $\omega_d$ are the linear natural frequency of the resonator and the base block in the discrete case, respectively.$\xi_d$,$\xi_1$ and $\xi_2$ are the damping ratios of two linear springs and the cantilever beam, respectively; $A$ is the amplitude of the excitation acceleration; $\mu^2$ is the mass ratio of the entire resonator to the base block; $\gamma_1$ is the coefficient representing the linear interaction between the resonator and the base block. Further, due to the large deformation bending and the tip block effect on the cantilever beam, the nonlinear terms appear in the governing equations and are labelled by $n_1$ and $n_2$ in Eq. (15), respectively. The bending deformation of the beam couples the motion of the tip block in the $x$ direction and the bottom block in the $y$ direction, with the coupling intensity characterized by the nonlinear coefficient $n_3$. Thus, the coefficients $n_1$, $n_2$ and $n_3$ are as follows. For convenience, $\phi$ is used to replace $\phi_1(s)$.

$$
\begin{cases}
n_1 = \displaystyle\int_0^l EI\left(\phi\phi'^2\phi''' + 4\phi\phi'\phi''' + \phi\phi''^3\right)ds \\
n_2 = \rho\displaystyle\int_0^L\left(\int_0^s \phi'(\eta)^2 d\eta\right)\phi'\phi\, ds - \int_0^L\left(\int_s^L \rho\left(\int_0^\xi \phi'(\eta)^2 d\eta\right)d\xi\right)\phi''\phi\, ds + M_2\left(\int_0^L \phi'^2 ds\right)\phi(L)\phi'(L) \\
\quad - \displaystyle\int_0^L\left(M_2\left(\int_0^L \phi'^2 ds\right) - 2L_c\phi'(L)^2\right)\phi\phi'' ds - 2M_2L_c\phi(L)\phi'(L)^3 + J_t\phi'(L)^4 \\
n_3 = M_2\left(\phi(L)\phi'(L) + L_c\phi'(L)^2\right) - \displaystyle\int_0^L M_2\phi''\phi\, ds + \int_0^L \rho\phi'\phi\, ds - \rho\int_0^L (L-s)\phi''\phi\, ds
\end{cases}
\tag{17}
$$

To facilitate the use of the Runge–Kutta method for solving the solutions of the system's governing equations, we introduce the following state space variables:

$$
Y = [Y_1, Y_2, Y_3, Y_4, Y_5, Y_6]^T = [y_d, \dot{y}_d, y_1, \dot{y}_1, q, \dot{q}]^T \tag{18}
$$

and rewrite the governing Eq. (15) as

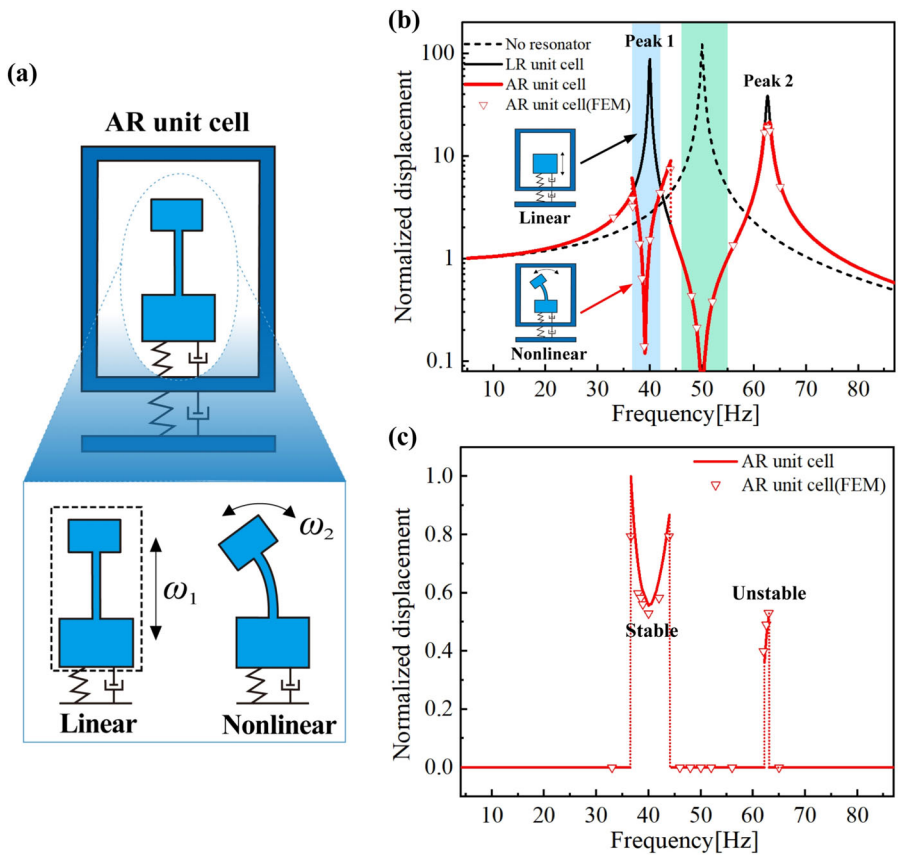


**Fig. 2** **a** The AR resonator with two modes, where the natural frequencies of the linear and nonlinear modes are denoted as $\omega_1$ and $\omega_2$, respectively; **b** Frequency–response curves of the base block, with resonator frequencies of $\omega_1 = 50$ Hz and $\omega_2 = 20.01$ Hz. The resonance peaks occur at $\Omega_1 = 39.95$ Hz and $\Omega_2 = 62.57$ Hz; **c** Frequency–response curves of the tip block

**Table 1** Material and geometric properties of the AR unit cell

| | | |
|---|---|---|
| $L_t$ | Length of the tip block [mm] | 5 |
| $L_c$ | Distance between the centre of the tip block and the beam's free end [mm] | 2.5 |
| $B_t$ | Width of the tip block [mm] | 10 |
| $L$ | Length of the beam [mm] | 30 |
| $B$ | Width of the beam [mm] | 1 |
| $E$ | Young's modulus of the beam [GPa] | 1.79 |
| $\rho$ | Mass per unit length of the beam [kg/m] | 0.00625 |
| $M_2$ | Mass of the tip block [g] | 4 |
| $M_1$ | Mass of the bottom block [g] | 4 |
| $M_d$ | Mass of the base block [g] | 40 |

$$\begin{aligned}
\dot{Y}_1 &= Y_2 \\
\dot{Y}_2 &= -\omega_d^2 Y_1 - 2\xi_1\gamma_1\mu(Y_2 - Y_4) - 2\xi_d\omega_d Y_2 - \gamma_1^2(Y_1 - Y_3) + A\cos(\omega t) \\
\dot{Y}_3 &= Y_4 \\
\dot{Y}_4 &= -\omega_1^2(Y_3 - Y_1) - 2\xi_1\omega_1(Y_4 - Y_2) + \frac{n_3}{M_1 + M_2 + M_c}\left(Y_5\dot{Y}_6 + Y_6^2\right) \\
\dot{Y}_5 &= Y_6 \\
\dot{Y}_6 &= -\omega_2^2 Y_5 - 2\xi_2\omega_2 Y_6 - n_1 Y_5^3 - n_2 Y_5(Y_5\dot{Y}_6 + Y_6^2) + n_3 Y_5\dot{Y}_4
\end{aligned} \tag{19}$$

The response of the system in a time domain can be calculated by solving Eq. (19), while the natural frequencies of the system can be determined by solving the eigenvalues of the linear matrix in the spatial state equation. The specific expression of the matrix is as follows:

$$\mathbf{B} = \begin{bmatrix}
0 & 1 & 0 & 0 & 0 & 0 \\
-\omega_d^2 - \gamma_1^2 & -2\xi_1\gamma_1\mu - 2\xi_d\omega_d & \gamma_1^2 & 2\xi_1\gamma_1\mu & 0 & 0 \\
0 & 0 & 0 & 1 & 0 & 0 \\
\omega_1^2 & 2\xi_1\omega_1 & -\omega_1^2 & -2\xi_d\omega_1 & 0 & 0 \\
0 & 0 & 0 & 0 & 0 & 1 \\
0 & 0 & 0 & 0 & -\omega_2^2 & -2\xi_2\omega_2
\end{bmatrix} \tag{20}$$

During the research process, the discrete frequency $\omega_d$ and the linear resonant frequency $\omega_1$ can be adjusted through the linear spring stiffness, the mass of the base block, and the total mass of the resonator. The resonant frequencies of the system can be obtained from Eq. (20). Furthermore, the natural frequency $\omega_2$ and the first-order mode shape $\phi_1(s)$ of the cantilever beam with the tip block can be obtained from Eq. (10–14). Finally, the nonlinear coefficients of the governing equations can be determined by Eq. (17). By adjusting the system's parameters, $\omega_2$ and the nonlinear coefficients can be tuned, enabling the investigation of the effects of autoparametric resonance on the resonance peaks in locally resonant metamaterials.

## 3 Results and verification

In this section, the effect of nonlinear coupling on resonance suppression is illustrated by comparing three cases of the unit cells: (i) no resonator, (ii) with a linear resonator, and iii) with a nonlinear resonator. Subsequent parametric analyses give insight into the effects of natural frequency and strength of nonlinearity on the nonlinear response.

### 3.1 Vibration suppression characteristics of AR unit cell

For the nonlinear AR unit cell, two modes of vibration of the resonator correspond to the linear and nonlinear modes respectively, as shown in Fig. 2a. The natural frequencies of the base block and linear mode are set as $\omega_d = \omega_1 = 50\text{Hz}$.

Then, using Eq. (12), (14) and (20), the natural frequencies of the system are obtained as $\Omega_1 = 39.95\text{Hz}, \Omega_2 = 62.57\text{Hz}$ and $\omega_2 = 20.01\text{Hz}$, where

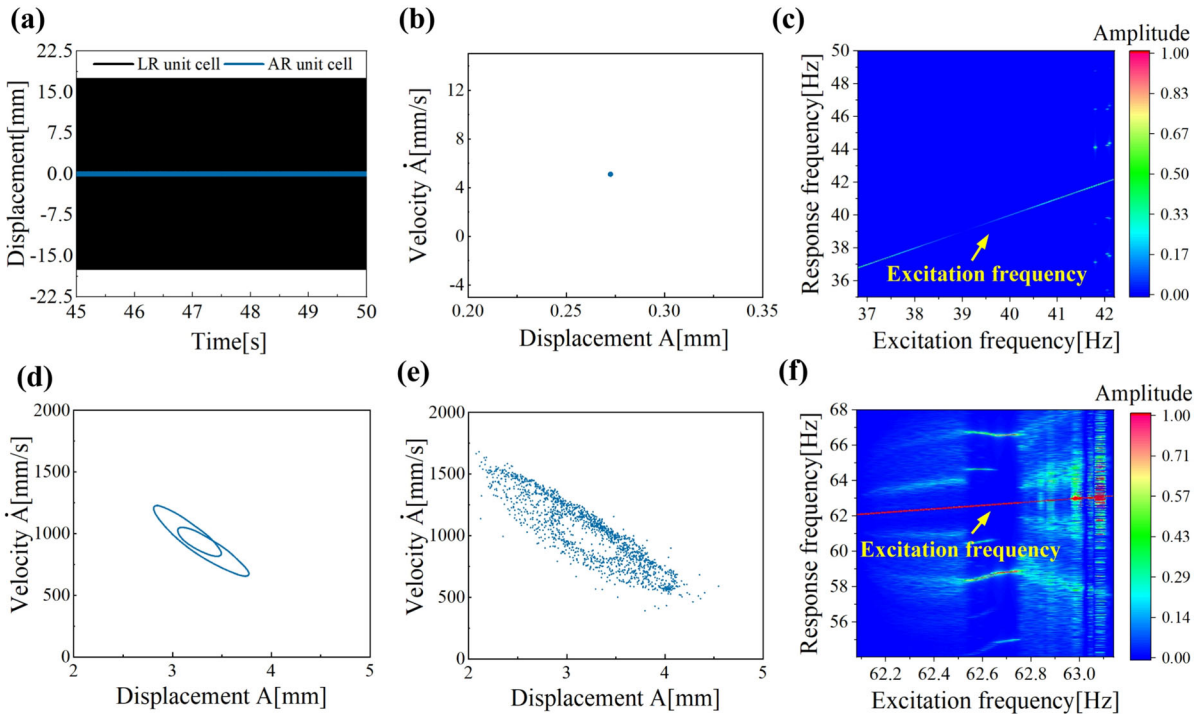


**Fig. 3** **a** and **b** Time histories and Poincaré section of the base block at the excitation frequency of $\Omega_1 = 39.95$ Hz; **c** Frequency spectra in the range of 36.8–42.2 Hz; **d** and **e** Poincaré section of the base block at the excitation frequency of $\Omega_2 = 62.57$Hz and 62.76 Hz; **f** Frequency spectra in the range of 62.08–63.17 Hz. In c and f, the red color exhibits high amplitude levels, while the blue color represents low amplitude levels. The frequency components corresponding to the excitation frequency are marked

$\Omega_1$ and $\Omega_2$ are the resonant frequencies of the locally resonant unit cell (LR unit cell),$\omega_2$ is the first-order natural frequency of the cantilever beam with the tip block, and it is also the natural frequency of the nonlinear mode. All material and geometric parameters of the prototype are given in Table 1.

Additionally, the excitation amplitude $A$ (Eq. (16)) is set to 19.5. To ensure the convergence of the solution, slight damping is added to the system. For the nonlinear response, the steady-state amplitude of the base block is evaluated using the root-mean-square (RMS) and then normalized by the static displacement ($F/k_d$).

The frequency–response results of the unit cell are shown in Fig. 2b. The lines represent the results calculated numerically by the Runge–Kutta method, and the dots represent the results simulated using the finite element software ANSYS. The details of the finite element model are provided in Appendix. It can be found that for the LR unit cell, when the excitation frequency equals the natural frequency of resonator, the spring force generated by the resonator counteracts the external force exerted on the primary mass, resulting in the primary mass remaining nearly stationary (damping is present). However, the introduction of the resonator causes the system's natural frequency to change from one to two, thereby generating two resonance peaks at $\Omega_1$ and $\Omega_2$, respectively. This is highly detrimental to effective vibration suppression.

While maintaining the total mass of the resonator constant, the AR unit cell, unlike the linear LR unit cell, retains the original linear vibration attenuation region, and the oscillation of the tip block in the deflection direction attenuates the two resonance peaks, as shown in Fig. 2b. When the excitation frequency is approximately twice $\omega_2$, as shown in Fig. 2c, the tip block begins to swing at the frequency of $\omega_2$ due to autoparametric resonance. Then, the nonlinear mode of the resonator is activated, and the tip block acts as a nonlinear resonator that absorbs energy from the base block. By transferring the energy

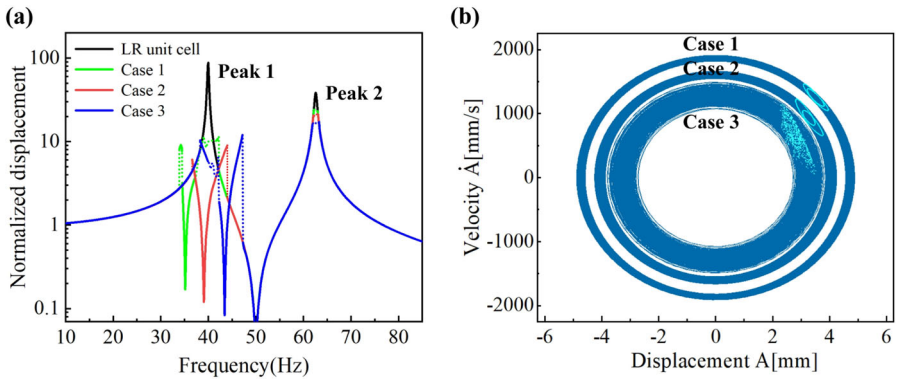


**Fig. 4** **a** Frequency–response curves at different $\omega_2$. From Case 1 to Case 3, $\omega_2$ are 17.55 Hz, 20.01 Hz, and 22.47 Hz; **b** Phase portraits and Poincaré sections at the excitation frequency of $\Omega_2 = 62.57$ Hz. The three concentric rings, with radii in descending order, correspond to Case 1, Case 2, and Case 3

to the tip block, the resonant amplitude of the base block decreases significantly, creating a new nonlinear vibration attenuation region between 36.7 and 42.12 Hz (blue shaded area in Fig. 2b), in which the amplitude of the nonlinear system is smaller than that of the LR unit cell.

When the excitation frequency is near $\omega_1$, the disproportionate frequency and smaller vibration amplitude cause the autoparametric resonance to fail, the nonlinear mode of the resonator vanishes, and the amplitude of the tip block in the deflection direction becomes zero. Then, the entire resonator exhibits the linear mode, where the tip block, cantilever beam, and bottom block can be regarded as a rigid system. The linear mode of the resonator produces a linear attenuation region with a frequency range that matches that of the linear system (green shaded area in Fig. 2b). The mode switching will produce the jump of the vibration amplitude (red dotted line in Fig. 2b and c), which is common in the autoparametric resonance systems [42].

When the excitation frequency is near $\Omega_2$, it is interesting that even though the excitation frequency does not satisfy the doubling relationship with $\omega_2$, the strong amplitude induced by the modal resonance still triggers autoparametric resonance, thereby weakening the amplitude near Peak 2. As shown in Fig. 2c, non-proportional frequencies will produce an unstable response between 62.1 and 63.13 Hz, in which there are no stable solutions.

Figure 3 illustrates the nonlinear vibration response of the base block within the two resonance peak regions. As shown in Fig. 3a and b, when the excitation frequency equal to $\Omega_1$, the amplitude of the base block is significantly attenuated, and the response exhibits periodic motion. Figure 3c depicts the frequency spectra of the base block within the nonlinear region near Peak 1. The results display that the energy at other frequencies is almost zero except for the dominant frequency, indicating that the vibration is essentially maintained in a stable motion.

When the excitation frequency equals to $\Omega_2$, the amplitude of resonance is also reduced. As depicted in Fig. 3d the Poincaré section becomes a closed orbit with one self-crossing, indicating that the base block undergoes a quasi-periodic response and stable torus motion. Upon further increasing the excitation frequency to 62.76 Hz, the orbit is destroyed and the points in Poincaré section become more irregular, as shown in Fig. 3e. Figure 3f presents the frequency spectra within the unstable response, and it can be observed that in addition to the dominant frequency, energy is also distributed across other frequencies. A more continuous distribution of amplitudes over the frequency range demonstrates the dispersion of energy. Subsequently, the response of the base block becomes random-like, and the system progressively shifts toward a chaotic response [55]. Finally, when the excitation frequency exceeds 63.13 Hz, the vibration returns to the periodic motion.

### 3.2 Effect of natural frequency of the nonlinear mode

To further illustrate the creation of resonance suppression, this section keeps other parameters constant and explores the influence of natural frequency of the nonlinear mode $(\omega_2)$ on the nonlinear response characteristics.

The frequency–response curves for three cases are shown in Fig. 4a. In these cases, the $\omega_2$ are equal to be 17.55 Hz, 20.01 Hz, and 22.47 Hz, respectively. The

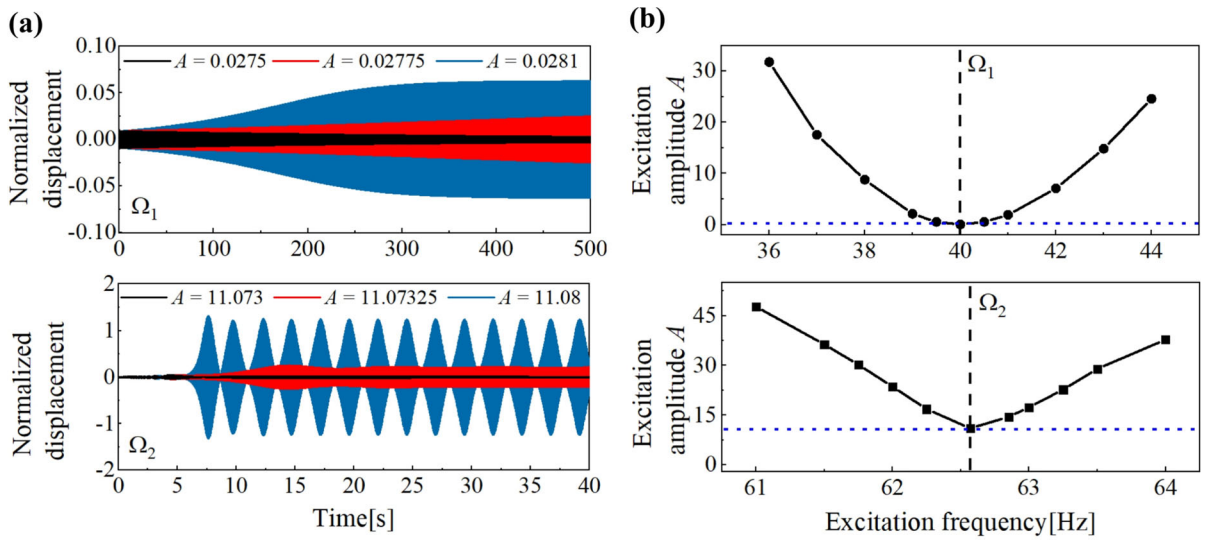


**Fig. 5** **a** The time histories of tip block under different excitation amplitudes $A$ when the excitation frequency is $\Omega_1 = 39.95$ Hz and $\Omega_2 = 62.57$ Hz; **b** The threshold of the excitation amplitude at different excitation frequencies. The dashed lines represent the excitation amplitudes $A$ corresponding to excitation frequencies $\Omega_1$ and $\Omega_2$

results indicate that the position of the nonlinear attenuation region is adjustable. This region is located at twice $\omega_2$ and does not affect the position of the linear attenuation region.

Within the nonlinear region, the response characteristics of the unit cell differ under the three cases. When the excitation frequencies are 35.14 Hz, 39.06 Hz, and 43.43 Hz, respectively, the three cases reach their minimum within the region. Moreover, as twice $\omega_2$ approaches $\omega_1$, the minimum amplitude becomes smaller. Due to the effect of nonlinear terms in Eq. (15), the excitation frequency of the minimum slightly deviates from twice $\omega_2$. Unlike the previous work [43], when two natural frequencies are present in the linear system, the asymmetry of the amplitude near Peak 1 is exacerbated. Consequently, as twice $\omega_2$ gets closer to $\omega_1$, the deviation of the excitation frequency becomes greater. Besides, when $\Omega_2$ and $\omega_2$ satisfy a double relationship, the conclusion remains the same.

For Case 1, when the excitation frequency increases to satisfy the condition of autoparametric resonance, the nonlinear mode is activated, and the system generates the jump up at 33.89 Hz, which results in a sudden increase in the amplitude of the unit cell. And for Case 3, the natural frequencies of the nonlinear mode and the linear mode are too close, resulting in a reduction of the linear attenuation region, which is undesirable. What is more, when the excitation frequency is near $\Omega_1$ in Case 1 and Case 3, the ratio of frequencies no longer complies with the doubling condition. The large vibration amplitude and frequency deviation result in the unstable response: 37.37–41.67 Hz in Case 1, and 39.92–42.25 Hz in Case 3, within which the response ceases to be periodic.

Meanwhile, the change of $\omega_2$ will also affect the nonlinear response near Peak 2. As $\omega_2$ increases, the response range of the autoparametric resonance expands from 62.34–62.92 Hz to 62–63.25 Hz. Additionally, the suppression effect on the resonant amplitude gradually strengthens. As shown in Fig. 4b, the Poincaré section transforms from the closed ellipse into a discrete set of points, indicating that the vibration response changes from quasi-periodic to chaotic.

### 3.3 Effect of excitation amplitude

In the previous section, we showed that when the excitation amplitude is large enough, autoparametric resonance can be excited to accomplish energy transfer even if the frequency ratio does not satisfy the doubling condition. Next, the natural frequencies of the system are kept at $\Omega_1 = 39.95$Hz, $\Omega_2 = 62.57$Hz and $\omega_2 = 20.01$Hz, and the influence of excitation amplitudes on the AR unit cell is explored.

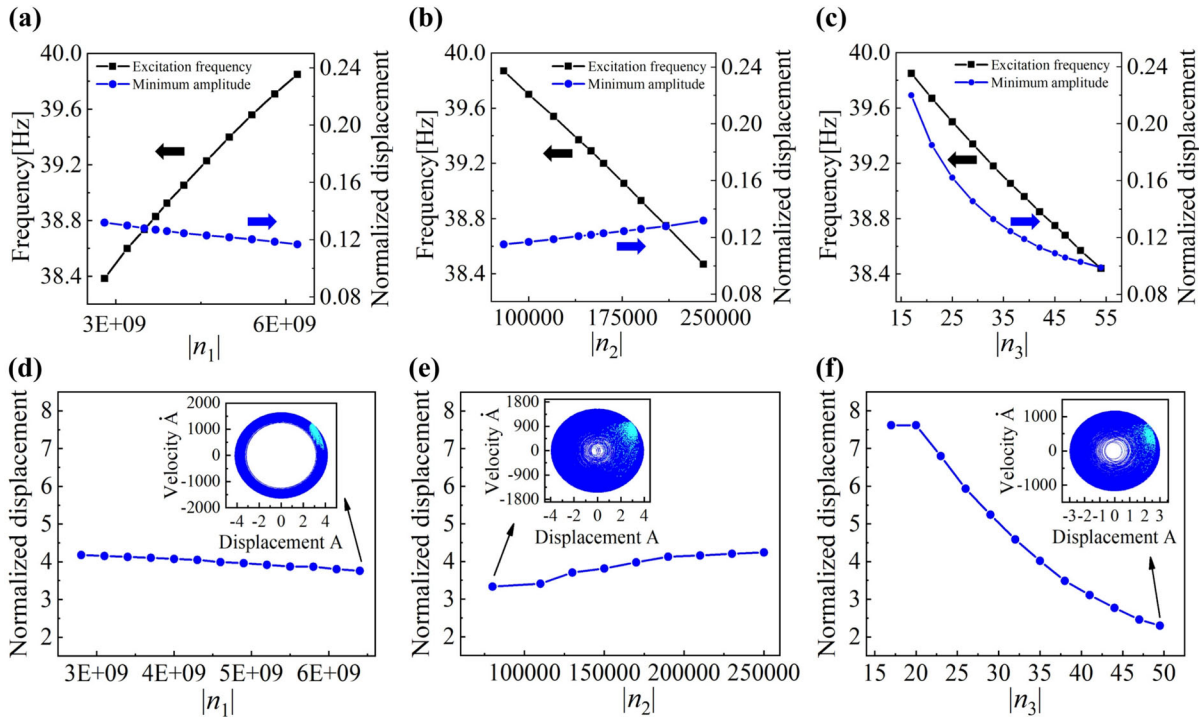


**Fig. 6** Effect of nonlinear coefficient $n_1, n_2$ and $n_3$ on vibration response of the base block. When one coefficient varies, the other coefficients remain unchanged ($n_1 = -4.1987\text{E}9, n_2 = 176361, n_3$=36.3071). **a–c** The minimum response amplitude within the valley and its excitation frequency; **d–f** Resonant amplitude at the excitation frequency of $\Omega_2 = 62.57$ Hz. The embedded figure shows the phase portraits and Poincaré sections of the base block under strong nonlinear conditions

Figure 5a shows the effect of excitation amplitude $A$ on the time histories of the tip block at the frequencies of two resonance peaks. When the excitation frequency $\Omega_1$ approximately satisfies the doubling relationship with the $\omega_2$, there is a threshold of the excitation amplitude that induces the tip block to oscillate periodically through the action of autoparametric resonance. When the excitation amplitude is very small ($A = 0.0275$), the oscillations of the resonator is insufficient to excite the nonlinear mode. As a result, the amplitude of the tip block decreases gradually due to the slight damping of the cantilever beam, and the resonator eventually returns to the linear mode. When the excitation amplitude is sufficiently large ($A = 0.0281$), the tip block absorbs energy and increases in amplitude, eventually resulting in a stable periodic response.

However, as depicted in the lower plot in Fig. 5a, when the excitation frequency is $\Omega_2$, the doubling condition for autoparametric resonance is no longer satisfied, requiring a larger amplitude of excitation to stimulate the tip block. Since the time histories exhibit periodic behavior, only the results for the time interval of 0–40 s are plotted. The results show that the nonlinearity of the system is also enhanced. The vibration response of the tip block passes from periodic to quasi-periodic with a small increase in the excitation amplitude. This also results in a decrease in the periodicity of the unit cell's output, leading to unstable response.

For the above two qualitatively different responses, Fig. 5b shows the threshold of the excitation amplitude that produces autoparametric resonance at different excitation frequencies. Using the bisection method, the intermediate state (tip block sustains oscillation) is selected as the criterion to determine the excitation threshold. It is found that in both cases, the required excitation amplitude is minimal at the resonant frequency; while increasing or decreasing the excitation frequency will both augment the threshold, and this effect is more pronounced when the frequency decreases. Compared to Peak 2, the

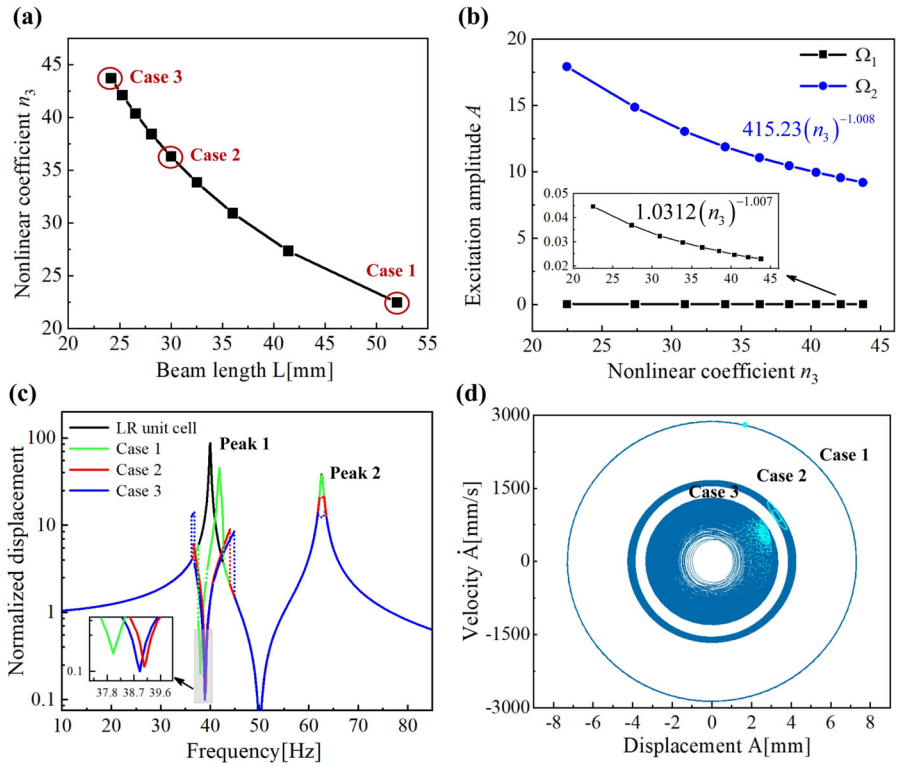


**Fig. 7** **a** Effect of beam length on the nonlinear coefficient $n_3$. From Case 1 to Case 3, $n_3$ are 22.46, 36.31 and 43.74; **b** The threshold of the excitation amplitude at different values of $n_3$, with excitation frequencies equal to the two resonance peaks,$\Omega_1 = 39.95$ Hz and $\Omega_2 = 62.57$ Hz; **c** Frequency–response curves at different strengths of nonlinearity, with resonator frequencies of $\omega_1 = 50$ Hz and $\omega_2 = 20.01$ Hz; **d** Phase portraits and Poincaré section of the three cases at the excitation frequency of $\Omega_2 = 62.57$ Hz. The three concentric rings, with radii in descending order, correspond to Case 1, Case 2, and Case 3

excitation threshold near Peak 1 is insignificant because the excitation frequency is well matched with twice $\omega_2$. In addition, the change trends of the thresholds are different in the two cases. When the deviation between the excitation frequency and the resonant frequency is the same, the threshold increment of Peak 2 is significantly greater than that of Peak 1.

### 3.4 Effect of strength of nonlinearity

Next, keeping the natural frequencies and excitation amplitude constant, the influence of different strengths of nonlinearity on the unit cell is explored. Based on Eq. (17), further investigation is carried out to explore the effects of the three nonlinear coefficients $n_1$, $n_2$, and $n_3$ on the vibration response.

First, from the previous conclusions, it can be observed that when the excitation frequency is approximately twice $\omega_2$, the autoparametric resonance creates an attenuation region (similar to a valley), where a minimum amplitude occurs within the interval. For the lowest point of the valley, Fig. 6a–c presents the effects of the three nonlinear coefficients $n_1$, $n_2$, and $n_3$ on the output amplitude and excitation frequency. When one nonlinear coefficient varies, the other coefficients remain unchanged. The initial parameter settings are as follows: $n_1 = -4.1987\text{E}9, n_2 = 176361, n_3$=36.3071. As shown in Fig. 6a and b, increasing $n_1$ or decreasing $n_2$ will further reduce the minimum amplitude within the valley, while the corresponding excitation frequency shifts to a higher frequency. In comparison, $n_3$ has a significantly greater impact on the linear system. As shown in Fig. 6c, increasing $n_3$ can more effectively reduce the amplitude while shifting the excitation frequency to a lower frequency.

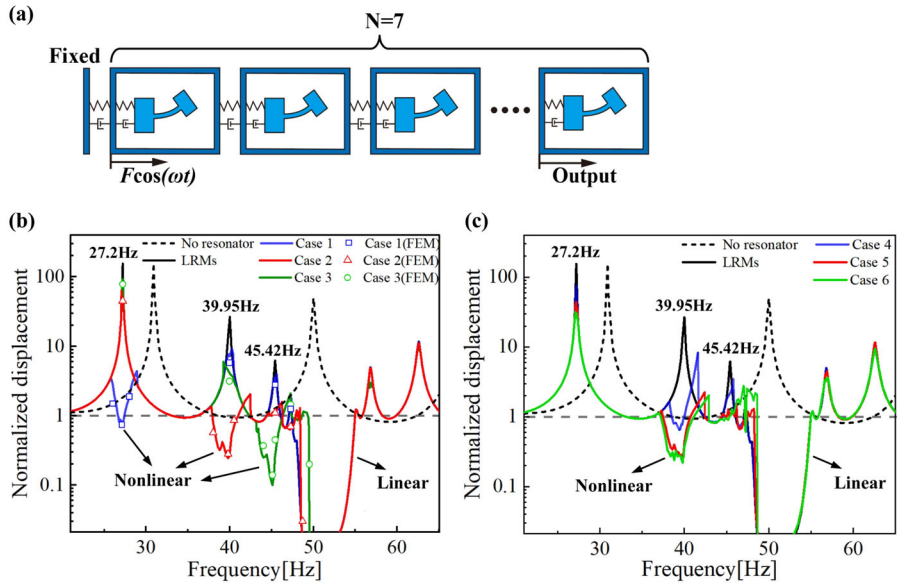


**Fig. 8** **a** Mechanical model of the ARMs with seven unit cells. The first unit cell is the input, and the seventh unit cell is the output; **b** Frequency–response curves of the output at different $\omega_2$. From Case 1 to Case 3, $\omega_2$ are 17.55 Hz, 20.01 Hz, and 22.47 Hz; **c** Frequency–response curves of the output at different strengths of nonlinearity. From Case 4 to Case 6, $n_3$ are 22.46, 36.31 and 43.74

When the excitation frequency equals $\Omega_2$, the frequency does not satisfy the doubling condition. As shown in Fig. 6d–f, increasing $n_1$or decreasing $n_2$ will also enhance the suppression of the resonance. Meanwhile, it decreases the periodicity of the oscillation, and leads to an unstable response. Similarly, the effect of $n_3$ on the resonant amplitude remains more pronounced. Therefore, in subsequent studies,$n_3$is used as a measure of strength of nonlinearity.

Subsequently, the system's strength of nonlinearity and natural frequency $\omega_2$ can be tuned by adjusting the geometric and physical parameters of the resonator. As shown in Fig. 7a, reducing the length of the cantilever beam can increase the nonlinear coefficient $n_3$, while adjusting the mass ratio of the tip block to the bottom block keeps $\omega_2$ at 20.01 Hz. Then, Fig. 7b depicts the threshold of the excitation amplitude at two resonant frequencies with different strengths of nonlinearity. In both cases, the threshold follows the same trend: as the nonlinearity increases, the required excitation amplitude to activate resonator's nonlinear mode decreases. Specifically, when the excitation frequency equals $\Omega_2$, the overall threshold is much larger than that of $\Omega_1$due to the disproportionate frequency relationship. Additionally, the power of the fitting functions is nearly identical, indicating that variations in the strength of nonlinearity have a comparable impact at the two resonant frequencies.

Figure 7c depicts the frequency–response curves for three cases of strength of nonlinearity, as marked in Fig. 7a. When the nonlinearity is weak, as in Case 1, the attenuation region becomes narrow. The nonlinear mode of the resonator is activated at 37.45 Hz, causing the amplitude of the unit cell to drop suddenly. As the excitation frequency is further increased, an unstable response is formed near Peak 1 (36.42–39.1 Hz), and when the frequency reaches 41.75 Hz, a new resonance peak is generated. When the nonlinearity is further increased, the range of the nonlinear response is broadened, and the suppression of resonance is simultaneously enhanced, without affecting the linear local resonance.

Additionally, increasing the strength of nonlinearity also broadens and enhances the suppression of Peak 2. Figure 7d displays the phase portraits and Poincaré section at $\Omega_2$ for the three cases. As the nonlinearity increases, the vibration amplitude and periodicity of the unit cell gradually decrease. Consequently, the system's response transitions from periodic to quasi-periodic and eventually to chaotic.

### 3.5 Vibration suppression characteristics of ARMs

The results from the analyses of the response of the unit cell reveal that the nonlinear effect of autoparametric resonance can effectively suppress the resonant

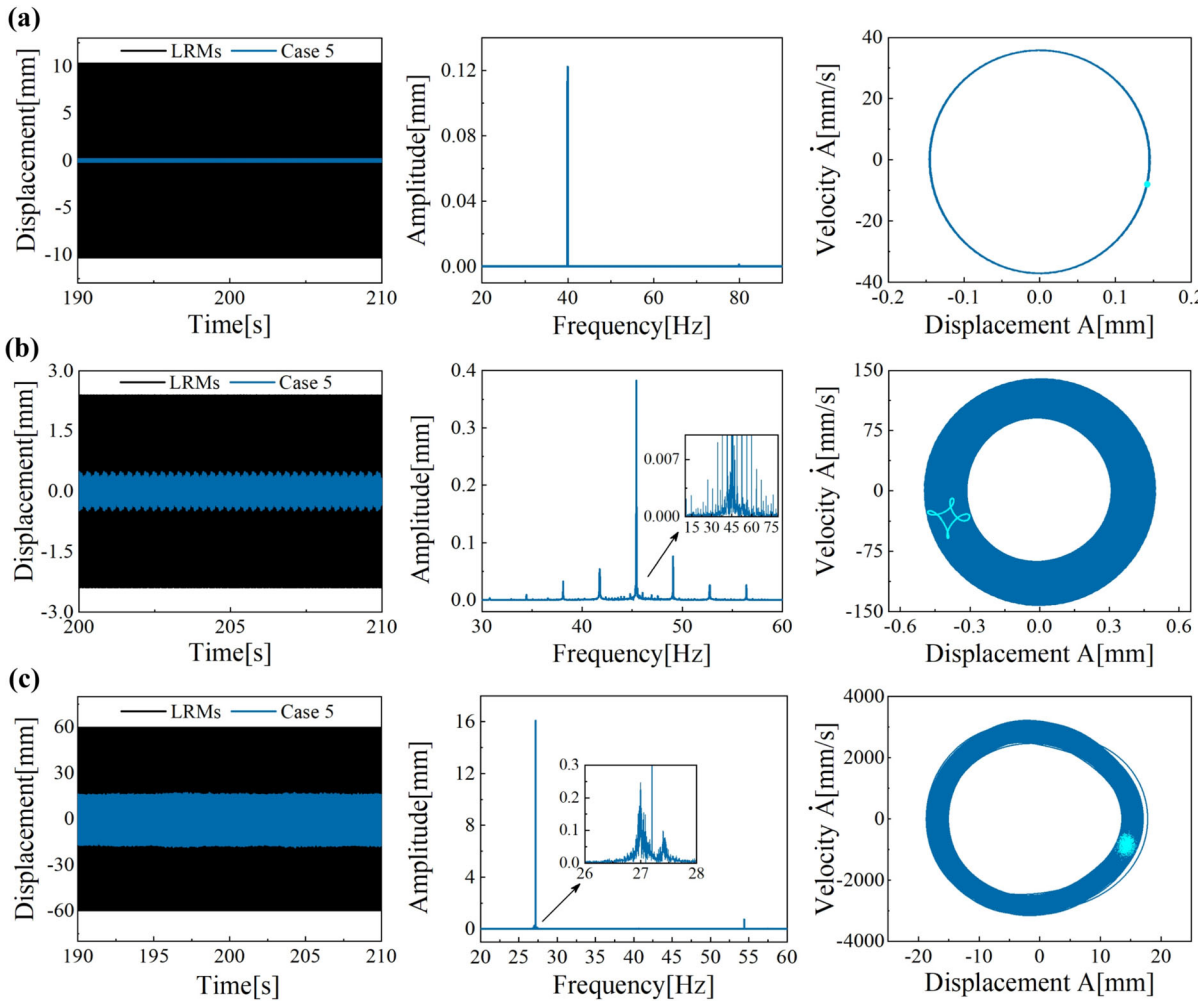


**Fig. 9** Time histories, amplitude spectra, phase portraits and Poincaré sections of the output response in Case 5 at different excitation frequency. **a** 39.95 Hz; **b** 45.42 Hz; **c** 27.2 Hz. The first column shows the time histories of LRMs and ARMs, the second column shows the amplitude spectra of ARMs, and the third column shows the phase portraits and Poincaré sections of ARMs

amplitude near the linear attenuation region, and a new nonlinear attenuation region is observed at twice $\omega_2$. In this section, we investigate the vibration suppression characteristics of the ARMs with multiple unit cells, limiting it here to seven unit cells. As shown in Fig. 8a, the leftmost end is as attached to a fixed base, while the rightmost end is free. Then, a harmonic force excitation is applied to the first unit cell as the input ($A$ = 37.5), and the normalized RMS of the last unit cell is the output.

Firstly, the $\omega_1$ of all resonators is equal to 50 Hz, and the $\omega_2$ is adjusted by changing the mass ratio of the tip block to the bottom block. Figure 8b displays the frequency response curves of ARMs at different $\omega_2$, with the results of finite element model represented by the dots. From Case 1 to Case 3, the $\omega_2$ are equal to 13.6 Hz, 20.01 Hz and 22.71 Hz respectively, while the nonlinear coefficient $n_3$ remains approximately 36.3. It is very apparent that for the LRMs, a linear bandgap is generated near the $\omega_1$; however, some resonance peaks also occur simultaneously outside the region.

For the ARMs, the nonlinear mode of the resonator is excited through autoparametric resonance, effectively attenuating the resonant amplitude. When the excitation frequency satisfies a doubling relationship

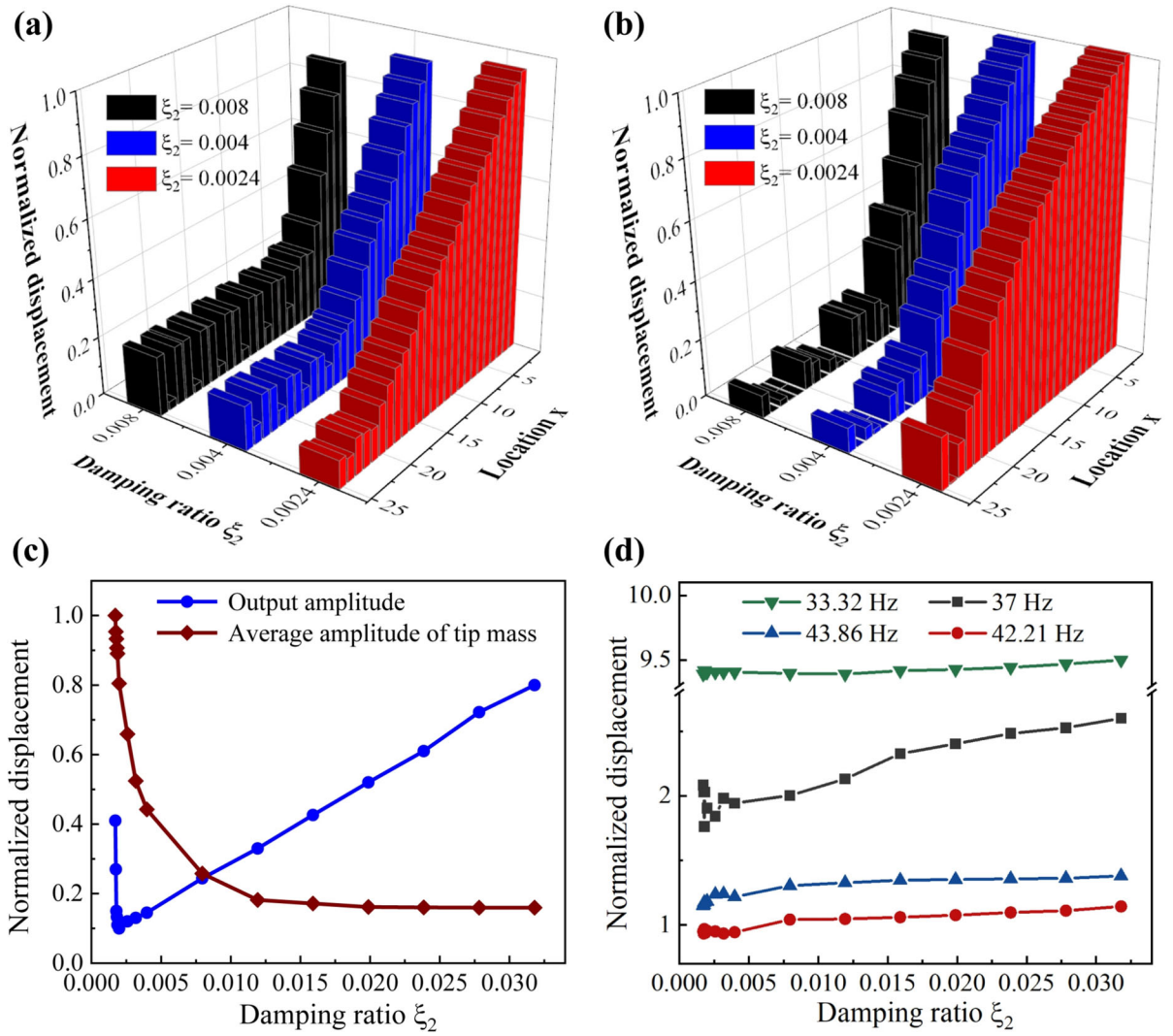


**Fig. 10** Influence of beam damping $\xi_2$ on the response of the 25-cell ARMs. **a** and **b** The amplitudes of the base block and tip block of each unit cell at the excitation frequency of 39.95 Hz. The location X represents the position of the unit cell within the metamaterial (X = 25 corresponds to the output); **c** The response of ARMs with different damping ratios $\xi_2$ at the excitation frequency of 39.95 Hz; **d** Output amplitude of ARMs with different damping ratios $\xi_2$ when resonant frequency does not satisfy the doubling condition. The excitation frequencies are 33.32 Hz, 37 Hz, 42.21 Hz, and 43.86 Hz, which correspond to the different resonance peaks shown in Fig. 11b

with $\omega_2$, the resonance peak is reduced to a valley, forming a new nonlinear vibration attenuation region, where the normalized amplitude is less than 1. Consistent with the unit cell, the closer twice $\omega_2$ is to $\omega_1$, the deeper the valley. Moreover, when the excitation frequency is not proportional, the amplitude of the resonance peaks outside the region is also attenuated. A comparison reveals that the smaller the deviation between the resonant frequency and twice $\omega_2$, the greater the attenuation of the resonant amplitude. When the excitation frequency is near $\omega_1$, autoparametric resonance fails. The nonlinear mode of resonators switches to the linear mode, which produces a linear locally resonant bandgap.

Additionally, since the directions of motion of the linear and nonlinear modes of the resonator are perpendicular to each other, the addition of the nonlinear mode does not increase the system's eigenmodes and therefore it does not produce new resonance peaks.

When the excitation amplitude is constant, the vibration energy gradually decreases during transmission. Since the occurrence of autoparametric resonance is related to the vibration amplitude of each unit cell, if the amplitude of the resonator is too small, the strength of nonlinearity is insufficient to drive the nonlinear mode, ultimately failing to form a bandgap like the LRMs. Next, the $\omega_2$ is maintained at 20.01 Hz, and the results for ARMs with different strengths of nonlinearity are shown in Fig. 8c. From Case 4 to Case 6, $n_3$ is equal to 22.46, 36.31 and 43.74 respectively. By comparing the three cases, it can be found that the stronger the nonlinearity, the range of nonlinear attenuation can be widened and the depth of the valley can be further increased. Besides, the suppression of resonance peaks outside the attenuation region is also improved.

Figure 9 shows the nonlinear response results of ARMs at different resonance frequencies in Case 5. When the excitation frequency is 39.95 Hz, the output response corresponds to a stable periodic curve, and its amplitude is significantly lower than the one of the LRMs, as shown in Fig. 9a. Increasing the excitation frequency to 45.42 Hz, which is the frequency that does not satisfy the double condition, as shown in Fig. 9b, the resonant amplitude is also effectively reduced. Simultaneously, the Poincaré section changes from a point to a closed orbit with several self-crossings, indicating the quasi-periodic motion. When the frequency deviation and vibration amplitude further increase, as shown in Fig. 9c, the response curve is more random, and the frequency in the power spectrum becomes continuous. The destruction of the torus in the Poincaré section shows that the system becomes chaotic.

## 4 Parameter design of ARMs

To overcome the limitations of the excitation amplitude and strength of nonlinearity of the metamaterial, this section aims at maximizing the effect of autoparametric resonance in the ARMs. Thus, it will be shown in this section that by adjusting the damping ratio of cantilever beam and the natural frequency of resonator's nonlinear mode, the ARMs can achieve a superior nonlinear suppression performance.

### 4.1 Effect of damping ratio

When the excitation amplitude and strength of nonlinearity are low, the nonlinear mode of the resonators cannot be fully excited, resulting in a relatively large output amplitude for the ARMs. The generation of autoparametric resonance depends not only on the strength of nonlinearity but also on the damping [56]. In this section, by maintaining other parameters constant, a smaller output amplitude can be achieved by adjusting the damping of the cantilever beam.

Firstly, the number of unit cells is set to 25, with $\omega_1$ and $\omega_2$ of resonators are equal to 50 Hz and 20.01 Hz respectively. When the excitation frequency is approximately twice $\omega_2$ (39.95 Hz), Fig. 10a illustrates the vibration amplitude of the base block of each unit cell for various damping ratio of the beam. The results indicate that with a higher damping ratio, the

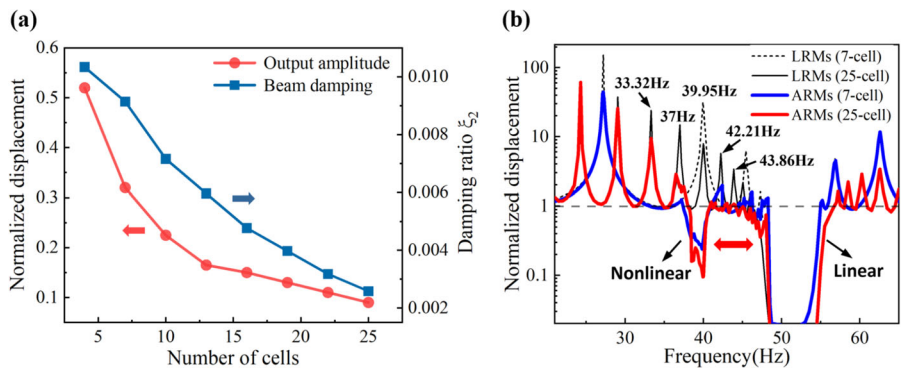


**Fig. 11** Influence of the number of unit cells on the response. **a** Optimal damping ratio $\xi_2$ of the beam and minimum output amplitude at the excitation frequency of 39.95 Hz; **b** Frequency–response curves of different metamaterials with 7 and 25 unit cells. The red arrows indicate the effective elimination of resonance peaks within this range

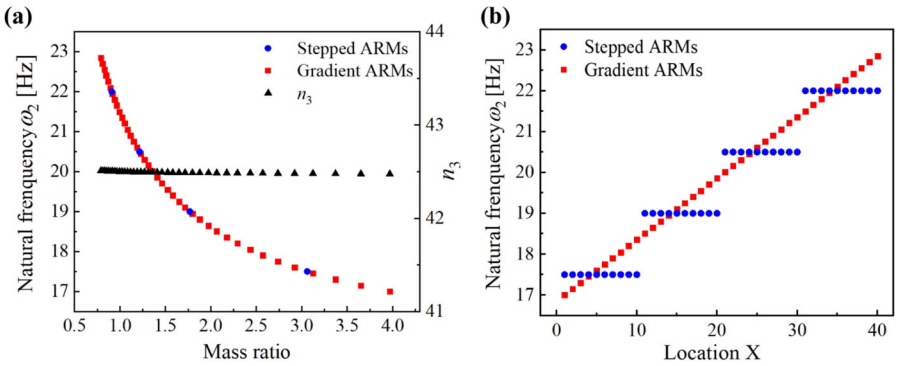


**Fig. 12** **a** Effect of mass ratio on the natural frequency $\omega_2$ and nonlinear coefficient $n_3$. The mass ratio is defined as the ratio of the tip block to the bottom block; **b** the $\omega_2$ of each resonator in the stepped ARMs and gradient ARMs. The location X represents the position of the unit cell within the metamaterial (X = 40 corresponds to the output)

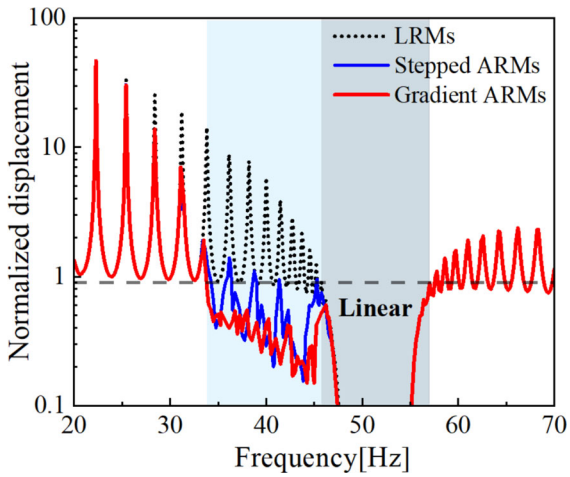


**Fig. 13** Frequency–response curves for different types of metamaterials. The dark shaded region represents the linear bandgap, while the light shaded region represents the nonlinear bandgap. All three metamaterials consist of 40 unit cells, with the resonator mass being identical

amplitude decreases rapidly along the metamaterials but remains at a high level. Conversely, reducing the damping ratio slows the rate of the amplitude reduction, resulting in a significant decrease in the final output amplitude. Figure 10b illustrates the corresponding amplitude of the tip block. A lower damping ratio reduces the amplitude threshold required for the resonators to activate the nonlinear mode, thereby increasing the number of tip blocks oscillating within the metamaterial. As shown in Fig. 10c, reducing the damping ratio can increase the average amplitude of the tip block and transfer more energy from the base block to the tip block. Consequently, the output amplitude at the resonant frequency is further effectively reduced. However, when the damping is too low, the vibration of the tip block cannot be sustained, causing energy to flow back to the base block, which results in an increase in the output amplitude. Therefore, it can be found that when the damping ratio is reduced to its optimal value, the output amplitude reaches its minimum.

Additionally, when the excitation frequency does not satisfy the doubling condition, as shown in Fig. 10d, reducing the damping ratio can also enhance the suppression of the resonance peaks outside the attenuation region. However, the corresponding impact is relatively small.

### 4.2 Effect of the number of unit cells

The number of unit cells in metamaterials also affects the suppression performance. When the excitation frequency is 39.95 Hz, Fig. 11a illustrates the optimal damping ratio and the corresponding output amplitude with a different numbers of unit cells. It is observed that increasing the number of unit cells reduces the optimal damping ratio while achieving a substantial reduction in the output amplitude. Figure 11b compares the frequency–response results of the ARMs with 7 and 25 unit cells at the optimal damping ratio. The results indicate that when the excitation frequency is within the nonlinear attenuation region, the 25-cell ARMs exhibit a smaller output amplitude compared to the 7-cell ARMs, with the minimum amplitude reduced from 0.25 to 0.095. Furthermore, when the excitation frequency does not satisfy the doubling

condition, the resonant amplitude between the nonlinear attenuation region and the linear bandgap is further effectively diminished.

### 4.3 Variable natural frequency

By optimizing the beam damping and the number of cells, a smaller output amplitude can be achieved. However, the range of the nonlinear attenuation region remains restricted. In this section, the nonlinear vibration attenuation regions and linear locally resonant bandgap are combined to create a broadband region for vibration suppression by adjusting the $\omega_2$ of resonators.

First, the total mass and $\omega_1$ of the resonator remain constant, while the $\omega_2$ is adjusted by varying the mass ratio of the tip block to the bottom block. As illustrated in Fig. 12a, the value of the $\omega_2$ decreases as the mass ratio increases, while the nonlinear coefficient $n_3$ remains almost unchanged ($n_3$= 42.5). As shown in Fig. 12b, the number of unit cells is set to 40, and the $\omega_2$ are designed with stepped and gradient variations, respectively. In both cases, the frequency intervals are 1.5 Hz and 0.15 Hz.

The frequency–response results of the different types of metamaterials are depicted in Fig. 13. The stepped and gradient designs can be interpreted as the discretization and continuousization of the natural frequency, respectively. Due to the nonlinear mode of the resonators, the stepped and gradient ARMs both exhibit the nonlinear vibration attenuation region at twice $\omega_2$, and the amplitude of resonance peaks outside the region is also reduced. However, the vibration isolation effect of the stepped design still requires improvement. Specifically, for the stepped ARMs, the gap between the natural frequencies of the nonlinear modes is relatively large. As a result, at certain excitation frequencies, the number of nonlinear unit cells responding in the system is relatively small, leading to a larger output amplitude. Consequently, some peaks may appear within the nonlinear bandgap. In contrast, gradient ARMs feature smoothly arranged natural frequencies $\omega_2$ within a certain frequency range, which can effectively eliminate the peaks present in the stepped ARMs. Each resonator in the metamaterial fully utilizes the effect of autoparametric resonance, and the nonlinear vibration attenuation region successfully merges with the linear locally resonant bandgap. Compared to the traditional LRMs, the overall width of the attenuation region is widened to 2.1 times of the original one.

## 5 Conclusion

To address the limitations of traditional linear locally resonant metamaterials, a nonlinear locally resonant metamaterial with autoparametric resonance characteristics has been proposed, which can effectively suppress the resonance peaks near the linear bandgap region while retaining the original linear locally resonant bandgap. Furthermore, several parameters, such as the natural frequency, the strength of nonlinearity, damping, and the number of unit cells, have been investigated to explore the effects on the attenuation of resonance peaks. Some conclusions can be drawn as follows:

(1) The resonator exhibits both linear and nonlinear modes, where the linear mode generates a linear locally resonant bandgap. When the excitation frequency is twice the natural frequency of the nonlinear mode, the autoparametric resonance generates a low-frequency nonlinear vibration attenuation region. The position and attenuation characteristics of this region can be independently adjusted by tuning the natural frequency of the resonator.

(2) When the excitation frequency does not satisfy the double relationship with the natural frequency of the nonlinear mode, a large amplitude of the resonance peak will induce an unstable response. The resonator's oscillation becomes quasi-periodic or chaotic, effectively suppressing the resonant amplitude outside the attenuation region. Besides, the smaller the deviation between the two frequencies, the stronger the suppression effect.

(3) Reducing the length of the cantilever beam can increase the strength of nonlinearity of the resonator, further enhancing the attenuation capability.

(4) By utilizing a smaller beam damping and a larger number of unit cells, the suppression effect can be effectively enhanced, significantly reducing the output amplitude of ARMs.

(5) The nonlinear vibration attenuation region and the linear locally resonant bandgap can be

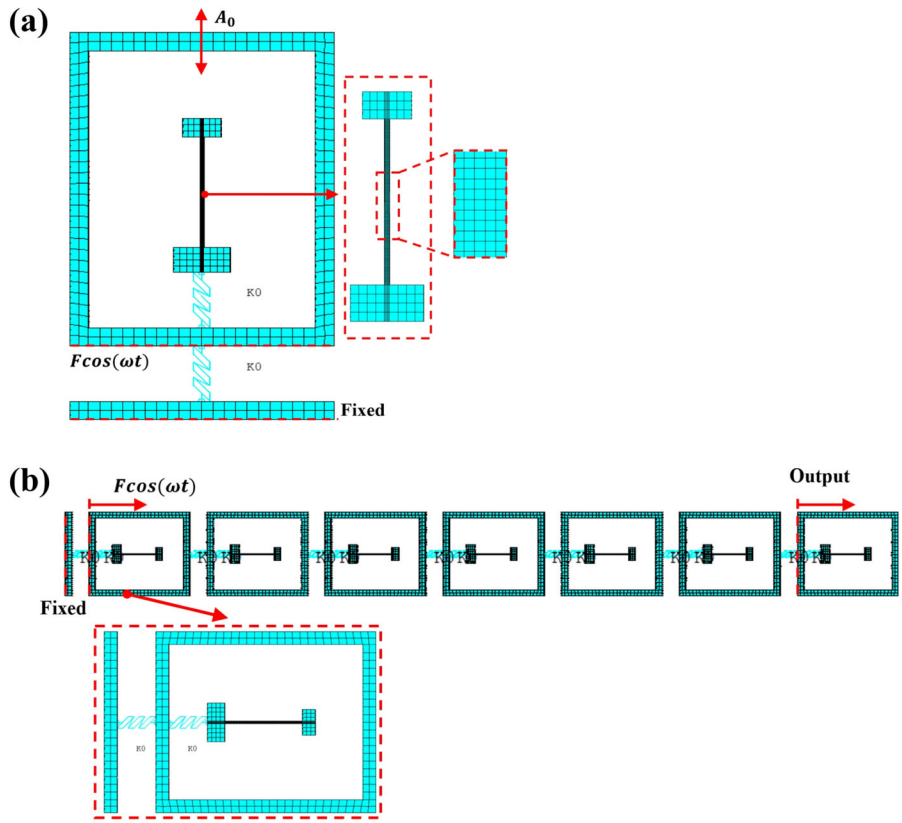


**Fig. 14** **a** FE model of AR unit cell using Plane183 element and Combin14 element; **b** FE model of ARMs with 7 unit cells

merged by designing a gradient in the natural frequencies of the resonators, thus greatly broadening the vibration suppression range.

Our work demonstrates that the proposed nonlinear metamaterial, without increasing the mass of the resonator, simultaneously features a linear bandgap and an independently adjustable nonlinear vibration attenuation region. Such metamaterial also effectively diminishes the resonant amplitude outside these regions. Future research will focus on the investigation of the exploitation of combination of other types of nonlinearities and autoparametric resonance for the sake of practically beneficial vibration suppression.

**Acknowledgements** This work was supported in part by the National Natural Science Foundation of China (NSFC) under Grants No. U22B2078, and in part by the National Key Research and Development Program of China under Grant No. 2021YFE0110900, and in part by the National Natural Science Foundation of China (NSFC) under Grants No. 11991033. The involvement of Ivana Kovacic was supported by the Ministry of Education, Science and Technological Development of the Republic of Serbia via the NOLIMAST project.

**Author contributions** X. Wang: conceptualization of the design, Theoretical analyses, Numerical analysis, Writing; J. Zhao: numerical analysis, Writing; I. Kovacic: theoretical analyses, Supervisor, Review & editing; H. Li: evaluation of the concept and numerical analyses; R. Hua: evaluation of the concept and numerical analyses; R. Zhu: conceptualization, Review & editing, Supervisor.

**Funding** National Natural Science Foundation of China (U22B2078), National Key Research and Development Program of China (2021YFE0110900), National Natural Science Foundation of China (11991033), Ministarstvo Prosvete, Nauke i Tehnološkog Razvoja, NOLIMAST.

**Data availability** Relevant data can be made available upon reasonable request.

**Declarations**

**Conflict of interests** The authors declare no competing interests.

## Appendix

During the simulation, all structural entities were modeled using the Plane183 element, including the Euler–Bernoulli beam, while the linear spring was modeled using the Combin14 element. The mesh elements of the cantilever beam were refined to ensure the accuracy of the simulation results (Fig. 14). The Beam188/189 elements were not selected because the theoretical model neglects shear deformation effects.

The simulation applies transient dynamic analysis, taking into account the large deformation of the beam. The bottom of the system is fixed, and a force excitation is applied to the base block. To align with the theoretical model, the constraints on both the base block and bottom block allow motion only along the direction of the spring, ultimately yielding the system's steady-state output amplitude.

## References


1. Wang, Y., Li, L., Hofmann, D., Andrade, J.E., Daraio, C.: Structured fabrics with tunable mechanical properties. Nature **596**, 238–243 (2021). https://doi.org/10.1038/s41586-021-03698-7
2. Krushynska, A.O., Janbaz, S., Oh, J.H., Wegener, M., Fang, N.X.: Fundamentals and applications of metamaterials: breaking the limits. Appl. Phys. Lett. **123**, 240401 (2023). https://doi.org/10.1063/5.0189043
3. Oudich, M., Assouar, M.B., Hou, Z.: Propagation of acoustic waves and waveguiding in a two-dimensional locally resonant phononic crystal plate. Appl. Phys. Lett. **97**, 193503 (2010). https://doi.org/10.1063/1.3513218
4. Kildal, P.-S., Alfonso, E., Valero-Nogueira, A., Rajo-Iglesias, E.: Local metamaterial-based waveguides in gaps between parallel metal plates. IEEE Antennas Wirel. Propag. Lett. **8**, 84–87 (2009). https://doi.org/10.1109/LAWP.2008.2011147
5. Cai, W., Chettiar, U.K., Kildishev, A.V., Shalaev, V.M.: Optical cloaking with metamaterials. Nat. Photon. **1**, 224–227 (2007). https://doi.org/10.1038/nphoton.2007.28
6. Chen, H., Chan, C.T.: Acoustic cloaking in three dimensions using acoustic metamaterials. Appl. Phys. Lett. (2007). https://doi.org/10.1063/1.2803315
7. Grimberg, R., Tian, G.-Y.: High-frequency electromagnetic non-destructive evaluation for high spatial resolution, using metamaterials. Proc. Royal Soc. A: Math. Phys. Eng. Sci. **468**, 3080–3099 (2012). https://doi.org/10.1098/rspa.2011.0666
8. Grimberg, R., Savin, A., Steigmann, R., Serghiac, B., Bruma, A.: Electromagnetic non-destructive evaluation using metamaterials. Insight-Non-Destr. Test. Cond. Monit. **53**, 132–137 (2011). https://doi.org/10.1784/insi.2011.53.3.132
9. Li, X., Yu, X., Chua, J.W., Lee, H.P., Ding, J., Zhai, W.: Microlattice metamaterials with simultaneous superior acoustic and mechanical energy absorption. Small **17**, 2100336 (2021). https://doi.org/10.1002/smll.202100336
10. Xiao, Z., Gao, P., He, X., Qu, Y., Wu, L.: Lightweight cellular multifunctional metamaterials with superior low-frequency sound absorption, broadband energy harvesting and high load-bearing capacity. Mater. Des. **241**, 112912 (2024). https://doi.org/10.1016/j.matdes.2024.112912
11. Gao, J., Zhou, J., Wang, Q., Wang, K., Lin, Q., Tan, D.: Design and optimization of quasi-zero-stiffness dual harvester-absorber system. Int. J. Mech. Sci. **273**, 109227 (2024). https://doi.org/10.1016/j.ijmecsci.2024.109227
12. Liu, Z., Zhang, X., Mao, Y., Zhu, Y.Y., Yang, Z., Chan, C.T., Sheng, P.: Locally resonant sonic materials. Science **289**, 1734–1736 (2000). https://doi.org/10.1126/science.289.5485.1734
13. Yao, S., Zhou, X., Hu, G.: Experimental study on negative effective mass in a 1D mass–spring system. New J. Phys. **10**, 043020 (2008). https://doi.org/10.1088/1367-2630/10/4/043020
14. Cai, C., Zhou, J., Wu, L., Wang, K., Xu, D., Ouyang, H.: Design and numerical validation of quasi-zero-stiffness metamaterials for very low-frequency band gaps. Composite Structures. **236**, 111862 (2020). https://doi.org/10.1016/j.compstruct.2020.111862
15. Huang, H.H., Sun, C.T., Huang, G.L.: On the negative effective mass density in acoustic metamaterials. Int. J. Eng. Sci. **47**, 610–617 (2009). https://doi.org/10.1016/j.ijengsci.2008.12.007
16. Kari, L.: Dynamic Vibration Absorbers. In: Crocker, M.J. (ed.) Handbook of Noise and Vibration Control. pp. 745–752. Wiley (2007)
17. Cveticanin, L., Mester, G.: Theory of acoustic metamaterials and metamaterial beams: an overview. Acta Polytech. Hungarica **13**(7), 43–62 (2016). https://doi.org/10.12700/APH.13.7.2016.7.3
18. Sun, H., Du, X., Pai, P.F.: Theory of metamaterial beams for broadband vibration absorption. J. Intell. Mater. Syst. Struct. **21**, 1085–1101 (2010). https://doi.org/10.1177/1045389X10375637
19. Pai, P.F., Peng, H., Jiang, S.: Acoustic metamaterial beams based on multi-frequency vibration absorbers. Int. J. Mech. Sci. **79**, 195–205 (2014). https://doi.org/10.1016/j.ijmecsci.2013.12.013
20. Zhu, R., Liu, X.N., Hu, G.K., Sun, C.T., Huang, G.L.: A chiral elastic metamaterial beam for broadband vibration suppression. J. Sound Vib. **333**, 2759–2773 (2014). https://doi.org/10.1016/j.jsv.2014.01.009
21. Rui, S., Zhang, W., Yu, R., Wang, X., Ma, F.: A multi-band elastic metamaterial for low-frequency multi-polarization vibration absorption. Mech. Syst. Signal Process. **216**, 111464 (2024). https://doi.org/10.1016/j.ymssp.2024.111464
22. Dwivedi, A., Banerjee, A., Adhikari, S., Bhattacharya, B.: Bandgap merging with double-negative metabeam. Mech. Res. Commun. **122**, 103889 (2022). https://doi.org/10.1016/j.mechrescom.2022.103889

23. Raghavan, L., Phani, A.S.: Local resonance bandgaps in periodic media: theory and experiment. J. Acoust. Soc. Am. **134**, 1950–1959 (2013). https://doi.org/10.1121/1.4817894
24. Ding, H., Chen, L.-Q.: Designs, analysis, and applications of nonlinear energy sinks. Nonlinear Dyn. **100**, 3061–3107 (2020). https://doi.org/10.1007/s11071-020-05724-1
25. Arnold, F.R.: Steady-state behavior of systems provided with nonlinear dynamic vibration absorbers. J. Appl. Mech. **22**, 487–492 (1955). https://doi.org/10.1115/1.4011141
26. Gatti, G.: Fundamental insight on the performance of a nonlinear tuned mass damper. Meccanica **53**, 111–123 (2018). https://doi.org/10.1007/s11012-017-0723-0
27. Casalotti, A., El-Borgi, S., Lacarbonara, W.: Metamaterial beam with embedded nonlinear vibration absorbers. Int. J. Non-Linear Mech. **98**, 32–42 (2018). https://doi.org/10.1016/j.ijnonlinmec.2017.10.002
28. Fang, X., Lacarbonara, W., Cheng, L.: Advances in nonlinear acoustic/elastic metamaterials and metastructures. Nonlinear Dyn. (2024). https://doi.org/10.1007/s11071-024-10219-4
29. Fang, X., Wen, J., Bonello, B., Yin, J., Yu, D.: Ultra-low and ultra-broad-band nonlinear acoustic metamaterials. Nat. Commun. **8**, 1288 (2017). https://doi.org/10.1038/s41467-017-00671-9
30. Fang, X., Sheng, P., Wen, J., Chen, W., Cheng, L.: A nonlinear metamaterial plate for suppressing vibration and sound radiation. Int. J. Mech. Sci. **228**, 107473 (2022). https://doi.org/10.1016/j.ijmecsci.2022.107473
31. Shen, N., Jiang, J., Zhang, F., Ding, M.: Nonlinear tunability of elastic waves in one-dimensional mass-spring lattices attached with local resonators. Aerospace **9**, 818 (2022). https://doi.org/10.3390/aerospace9120818
32. Fiore, S., Finocchio, G., Zivieri, R., Chiappini, M., Garescì, F.: Wave amplitude decay driven by anharmonic potential in nonlinear mass-in-mass systems. Appl. Phys. Lett. **117**, 124101 (2020). https://doi.org/10.1063/5.0020486
33. Xia, Y., Ruzzene, M., Erturk, A.: Dramatic bandwidth enhancement in nonlinear metastructures via bistable attachments. Appl. Phys. Lett. **114**, 093501 (2019). https://doi.org/10.1063/1.5066329
34. Zhao, J., Zhou, H., Yi, K., Kovacic, I., Zhu, R.: Ultra-broad bandgap induced by hybrid hardening and softening nonlinearity in metastructure. Nonlinear Dyn. **111**, 17687–17707 (2023). https://doi.org/10.1007/s11071-023-08808-w
35. Yu, M., Fang, X., Yu, D.: Combinational design of linear and nonlinear elastic metamaterials. Int. J. Mech. Sci. **199**, 106422 (2021). https://doi.org/10.1016/j.ijmecsci.2021.106422
36. Chen, B., Zheng, Y., Dai, S., Qu, Y.: Bandgap enhancement of a piezoelectric metamaterial beam shunted with circuits incorporating fractional and cubic nonlinearities. Mech. Syst. Signal Process. **212**, 111262 (2024). https://doi.org/10.1016/j.ymssp.2024.111262
37. Zhao, T., Yang, Z., Tian, W.: Tunable nonlinear metastructure with periodic bi-linear oscillators for broadband vibration suppression. Thin-Walled Struct. **191**, 110975 (2023). https://doi.org/10.1016/j.tws.2023.110975
38. Kurmann, L.C.: Introduction to parametric and autoparametric resonance. Resonance (2017). https://doi.org/10.5772/intechopen.70521
39. Wang, Y.-Z.: Nonlinear internal resonance of double-walled nanobeams under parametric excitation by nonlocal continuum theory. Appl. Math. Model. **48**, 621–634 (2017). https://doi.org/10.1016/j.apm.2017.04.018
40. Jin, Q., Yuan, F.-G., Ren, Y.: Auto-parametric resonance of flexible viscoelastic beams under interaction between longitudinal and transverse modes. Chaos, Solitons Fract. **174**, 113880 (2023). https://doi.org/10.1016/j.chaos.2023.113880
41. Nayfeh, A.H., Lacarbonara, W., Chin, C.-M.: Nonlinear normal modes of buckled beams: three-to-one and one-to-one internal resonances. Nonlinear Dyn. **18**, 253–273 (1999). https://doi.org/10.1023/A:1008389024738
42. Haxton, R.S., Barr, A.D.S.: The autoparametric vibration absorber. J. Eng. Ind. **94**, 119–125 (1972). https://doi.org/10.1115/1.3428100
43. Yan, Z., Taha, H.E., Tan, T.: Nonlinear characteristics of an autoparametric vibration system. J. Sound Vib. **390**, 1–22 (2017). https://doi.org/10.1016/j.jsv.2016.12.003
44. Vyas, A., Bajaj, A.K., Raman, A.: Dynamics of structures with wideband autoparametric vibration absorbers: theory. Proc. Royal Soc. Lond. Ser. A: Math. Phys. Eng. Sci. **460**, 1547–1581 (2004). https://doi.org/10.1098/rspa.2003.1204
45. Yu, T., Cheng, Y., Zhou, S.: Non-reciprocity in nonlinear chirality-induced autoparametric periodic structures. Mech. Syst. Signal Process. **165**, 108325 (2022). https://doi.org/10.1016/j.ymssp.2021.108325
46. Zhou, S., Zhang, R., Cheng, Y., Yu, T.: Non-reciprocity and selective wave amplification in nonlinear inertia-induced autoparametric periodic structures. Appl. Math. Model. **130**, 457–471 (2024). https://doi.org/10.1016/j.apm.2024.03.005
47. Silva, P.B., Leamy, M.J., Geers, M.G.D., Kouznetsova, V.G.: Emergent subharmonic band gaps in nonlinear locally resonant metamaterials induced by autoparametric resonance. Phys. Rev. E **99**, 063003 (2019). https://doi.org/10.1103/PhysRevE.99.063003
48. Nayfeh, A.H., Pai, P.F.: Linear and nonlinear structural mechanics. John Wiley & Sons (2008)
49. Meesala, V.C., Hajj, M.R.: Parameter sensitivity of cantilever beam with tip mass to parametric excitation. Nonlinear Dyn. **95**, 3375–3384 (2019). https://doi.org/10.1007/s11071-019-04760-w
50. Li, J., Li, S., He, X., Yang, X., Ye, Y., Li, J.: Geometrically nonlinear model of piezoelectric wind energy harvesters based on vortex-induced vibration and galloping. Smart Mater. Struct. **31**, 105019 (2022). https://doi.org/10.1088/1361-665X/ac8efa
51. Huang, W., Chen, Z., Lin, W., Wang, S., Xie, Z.: A novel two degree of freedom single magnet bistable energy harvester based on internal resonance. Smart Mater. Struct. **32**, 015012 (2022). https://doi.org/10.1088/1361-665X/aca7a4
52. Li, J., He, X., Yang, X., Liu, Y.: A consistent geometrically nonlinear model of cantilevered piezoelectric vibration energy harvesters. J. Sound Vib. **486**, 115614 (2020). https://doi.org/10.1016/j.jsv.2020.115614
53. Abdelkefi, A., Yan, Z., Hajj, M.R.: Temperature impact on the performance of galloping-based piezoaeroelastic energy harvesters. Smart Mater. Struct. **22**, 055026 (2013). https://doi.org/10.1088/0964-1726/22/5/055026
54. Tan, T., Yan, Z., Lei, H., Sun, W.: Geometric nonlinear distributed parameter model for cantilever-beam

piezoelectric energy harvesters and structural dimension analysis for galloping mode. J. Intell. Mater. Syst. Struct. **28**, 3066–3078 (2017). https://doi.org/10.1177/1045389X17704922
55. Nayfeh, A.H., Balachandran, B.: Applied nonlinear dynamics: analytical, computational, and experimental methods. John Wiley & Sons (2008)
56. Zhang, C., Yabuno, H., Yasui, K.: Improving the performance of an autoparametric vibration absorber. Nonlinear Dyn. **112**, 10739–10758 (2024). https://doi.org/10.1007/s11071-024-09483-1